2011

Los Alamos Space Weather Summer School Research Reports

Josef Koller, *Editor*

2011

Los Alamos Space Weather Summer School
Research Reports

Josef Koller, *Editor*

2011

Los Alamos Space Weather Summer School Research Reports

Preface

When the Institute of Geophysics and Planetary Physics (IGPP) at Los Alamos National Lab sent out an announcement soliciting ideas for energizing their program, I suggested organizing a summer school for space weather sciences. It is interesting to note, as I found out later, that there were a total of 16 summer schools with topics on solar, space, and upper atmospheric physics worldwide. In spite of the large number of apparently similar programs, the Los Alamos Space Weather Summer School is unique by setting the following two goals: (1) to bring together top space science graduate students with Los Alamos researchers to create a pipeline of highly qualified postdocs for our space situational awareness program; and (2) to strengthen the collaboration between Los Alamos scientists and universities leading to new joint projects.

The idea of a space weather summer school in Los Alamos was well received by management and was honored with support from IGPP and the Principal Associate Directorate for Science, Technology and Engineering (PADSTE) at Los Alamos. A nationwide search for highly qualified candidates commenced and a panel reviewed all applicants and selected the top six graduate students to receive a prestigious Vela Fellowship for attending the summer school. The first summer school was in session from June 6 to July 29, 2011.

There was amazing support from the Space Science and Applications group office and the IGPP group office. The response from my colleagues was overwhelming: Everyone I approached wanted to teach some lectures. We ended up with a series of 22 lectures spread over seven weeks ranging from plasma waves and instabilities, statistics for space science, magnetospheric storms and substorms, spacecraft charging, astrodynamics, Python programming for space scientists, and many more.

Since the summer school follows a dual-track approach of lectures and research projects spread out over eight weeks, the students spent the majority of their time not in class but working on a research project mentored by a leading LANL scientist. The research projects were intended to allow the student to experience the broad range of scientific research at LANL and included a variety of topics ranging from plasma physics, solar energetic particles to radiation detectors and substorm injections.

2011

Los Alamos Space Weather Summer School Research Reports

At the conclusion of the summer school, all students presented their research. All students wrote up a report and this is the collection of all their papers. Due to the brevity of the summer school, most reports are describing work-in-progress but all of them clearly demonstrate the remarkable accomplishments of every student. A panel selected the best presentation, given by Miles Engel (Dartmouth College), who received an all-expenses paid trip to the Fall Meeting of the American Geophysical Union in San Francisco.

The summer of 2011 marked the first Los Alamos Space Weather Summer School. Many will remember it as the year of the Las Conchas Fire in July. In spite the mandatory evacuation of Los Alamos for seven days, the summer school was still a full success. The students learned an amazing amount in the lectures and experienced excellent hands-on research at LANL. Many new relationships and collaborations have been fostered and some of the research has already been submitted to peer-reviewed journals. In conclusion, the Los Alamos Space Weather Summer School is successfully establishing itself as (1) creating a pipeline of highly qualified and trained postdocs for our space situational awareness program and (2) developing new University collaborations leading to future joint projects.

Los Alamos, NM
December 2011

Dr. Josef Koller
Summer School Director

2011

Los Alamos Space Weather Summer School Research Reports

Students

Alex Boyd	*University of New Hampshire*
Ouliang Chang	*University of Southern California*
Justin Elfritz	*West Virginia University*
Miles Engel	*Dartmouth College*
Sun-Hee Lee	*University of Alaska at Fairbanks*
Liheng Zheng	*Rice University*

Lectures

• Plasma Waves and Instabilities	*Peter Gary*
• Magnetospheric Overview	*Geoff Reeves*
• Spacecraft Environment and Charging	*Joe Borovsky*
• Magnetospheric Storms	*Vania Jordanova*
• Plasma Sheets and Substorms	*Sorin Zaharia*
• Particle Transport and Adiabatic Conversion	*Mike Henderson*
• Ionospheric Outflow	*Dan Welling*
• Orbital Dynamics	*Alan Lovell, AFRL*
• Data Assimilation	*Humberto Godinez*
• Statistics for Space Science	*Steve Morley*
• Python for Space Science	*John Niehof*

2011

Los Alamos Space Weather Summer School
Research Reports

Pictures

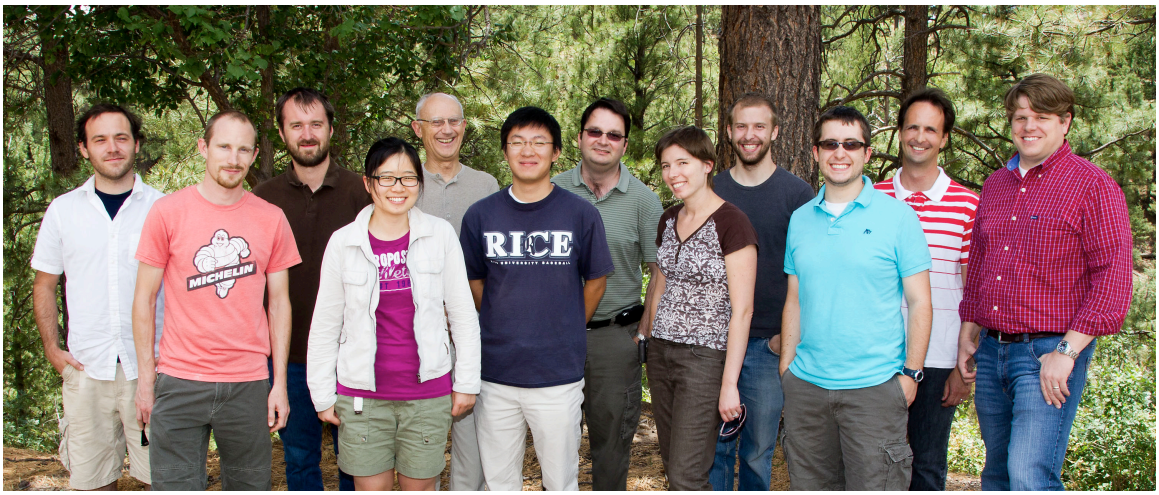

Class of 2011:
Front row from left to right: Steve Morley, Sun-Hee Lee, Liheng Zheng, Laura Stonehill, Alex Boyd, Russ Terry
Back row from left to right: Justin Elfritz, Brian Larsen, Peter Gary, Sorin Zaharia, Miles Engel, Josef Koller; (absent: Ouliang Chang)

LOS ALAMOS
SPACE WEATHER
SUMMER SCHOOL

2011

Los Alamos Space Weather Summer School
Research Reports

Sponsors

- Institute of Geophysics and Planetary Physics
- Principal Associate Directorate for Science, Technology and Engineering

Contact Information

Dr. Josef Koller
Los Alamos Space Weather Summer School
P.O. Box 1663, MS D466
Los Alamos National Lab, NM 87545

http://SpaceWeatherSchool.org

Publication Release

LA-UR 12-00074
ISBN 978-0-9850208-0-4 (paperback)
ISBN 978-0-9850208-1-1 (electronic)

2011

Los Alamos Space Weather Summer School
Research Reports

Project Reports

Scintillating and Solid-State Radiation Detectors
Mentor: Laura Stonehill; Russ Terry
Student: Alex Boyd 1

PIC Code Simulation of whistler turbulence
Mentor: Peter Gary
Student: Ouliang Chang 5

*Third Adiabatic Invariant L**
Mentor: Jon Niehof
Student: Justin Elfritz 13

Solar Energetic Particle Events
Mentor: Brian Larsen
Student: Miles Engel 19

Exploring the Relationship Between Substorm Injections and EMIC Waves
Mentor: Steve Morley
Student: Sun-Hee Lee 26

The Magnetospheric Magnetic Field During the Substorm Growth Phase
Mentor: Sorin Zaharia
Student: Liheng Zheng 34

Preparing to Investigate the Proton Response of CLYC

Alexander Boyd

Space Science Center, University of New Hampshire, Durham, NH 03824.

Laura Stonehill, Russell Terry

Space Science Applications Group, Los Alamos National Lab, Los Alamos, NM 87545

Abstract

Cs_2LiYCl_6:Ce (CLYC) is a new scintillating material useful for detection of both ionizing radiation and thermal neutrons. Using pulse shape discrimination (PSD), CLYC is able to distinguish between these particles. While the response of CLYC to neutrons, electrons and gamma rays is well understood, the response of to protons is not. To prepare for testing this response at the Ion Beam Materials Laboratory, this study focuses on calibration and development of new techniques for PSD. The result from both of these studies is encouraging, but more work will be needed to make these useful for further CLYC studies. In addition, the attenuation effect of batteries in the handheld neutron detector application of CLYC is discussed. The batteries seem to cause a significant decrease in neutron count rate, an effect that will need to be looked at in more detail.

Citation: Boyd, A., L. Stonehill, and R. Terry (2011), Preparing to Investigate the Proton Response of CLYC, Los Alamos Space Weather Summer School Reports 2011, pp. 1–4, LA-UR 12-00074, ISBN 978-0-9850208-1-1

Keywords: CLYC, Pulse Shape Discrimination, Scintillator

1. Introduction

Development of new radiation detection materials is an important topic in space physics. For high energy radiation, scintillating materials coupled with photomultiplier tubes are the detectors of choice. One emerging scintillating material is Cs_2LiYCl_6:Ce (CLYC). CLYC is not only effective at detecting ionizing radiation but is also able to detect thermal neutrons through capture on Lithium-6. Most importantly, CLYC is able to distinguish between neutrons and Electrons/Gamma Rays using Pulse Shape Discrimination (PSD). This is due to the differences in the way radiation behaves in the crystal. The Li-6 capture of thermal neutron results in the production of an alpha particle and a triton, which are heavy charged particles that ionize the particles in the scintillating crystal as they slow down. This process is different for or gamma rays and electrons, as they undergo photoelectric absorption and scattering. This leads to different rise and fall times in the response of the crystal that can be detected using PSD.

While the response to neutrons, gamma rays and electrons is well understood (Glodo et al., 2007, 2008), the response of CLYC to protons is unclear. In particular it remains unclear whether or not the pulse shapes of the protons and the neutrons would be sufficiently different to distinguish between them. Investigating the response of protons would also offer insight into how the neutron interacts with the crystal, showing whether the triton (similar to the proton) or the alpha particle is more important.

To test the proton response, a CLYC crystal will be taken to the Ion Beam Materials Lab (IBML) at Los Alamos National Lab. IBML uses a 3 MV Tandem Van de Graff Generator to create a beam of up to 6 MeV protons. In order to understand the results of this testing, the CLYC crystal must be properly calibrated using known sources. This report focuses on this preparation.

Email addresses: a.j.boyd@unh.edu (Alexander Boyd), lauracs@lanl.gov, rterry@lanl.gov (Laura Stonehill, Russell Terry)

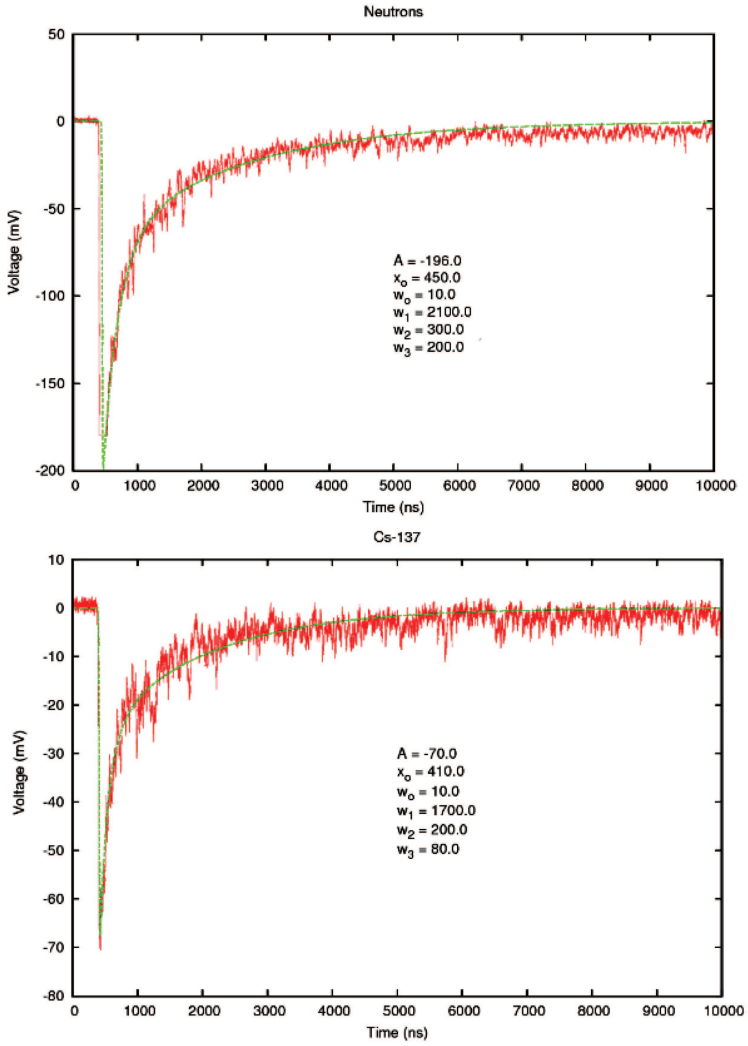

Figure 1: Curve fits for waveforms from a neutron and Cs-137 source. The fit parameters for each curve are listed

2. Pulse Shape Discrimination

Traditionally, the PSD is performed by taking the ratio of different integration windows of the waveform. Since neutrons and gammas/electrons have different rise times and fall times, these ratios are different for the two types of particles. For protons, it is unclear whether the waveform would be different enough from the neutron waveform for this technique to work. To resolve this, a curve can be fit to each of the pulse shapes. Then, the differences between the fit parameters will show subtle difference between the different particles spectra. Equation (1) shows the form of the fit that was used.

$$y = A * erf(\frac{x - x_0}{w_0})[\exp \frac{x - x_0}{w1} + \exp \frac{x - x_0}{w_2} + \exp \frac{x - x_0}{w_3}] \quad (1)$$

For the fit, the values for A and x_0 are fixed by the curve amplitude (A) and peak position (x_0). The rest of the parameters are calculated to offer the best match for each curve. An example of a fit for a neutron source and a Cs-137 source are shown in Figure 1. At this time, these values are calculated manually for each curve. Given the number of waveforms that need to be fit using this technique, it will need to become automated to be effective. However, early results show that neutrons and gamma rays have distinct ranges of parameters, indicating this could be an effective technique for PSD.

3. Calibration

In order to get an energy spectrum for CLYC, the response of the crystal needs to be found using known radiation sources. For this study, Cs-137, Co-60, and Na-22 were used as energetic gamma sources. The response of the instrument to the Cs-137 source, in counts vs. channel, is shown in Figure 2. In order to be useful, the spectrum must be converted into counts vs. energy. Since the energy of the photopeak for Cs-137 is known (662 keV), this gives a pairing between the channel number and photon energy. Repeating the process for Na-22 and Co-60 gives a series of points that be fitted to give a linear relation between chanel and photon energy. Using this correlation, the energy spectrum for Cs-137 can be found. It is shown in Figure 3. From the Cs-137 spectrum, the energy resolution is 7.4%, which is in line with previous studies on CLYC.

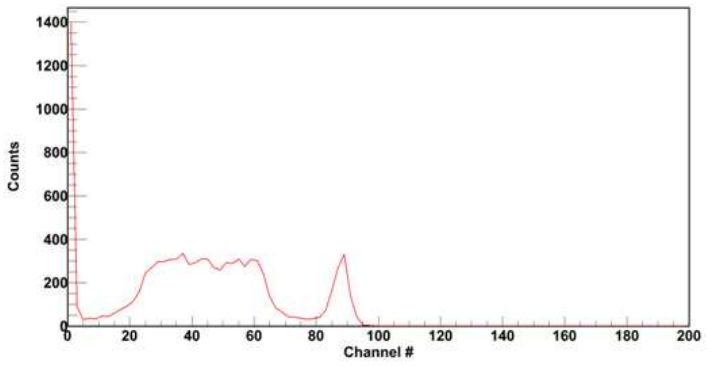

Figure 2: Uncalibrated spectrum for Cs-137 Source. Peak in the spectrum is the 662 keV photopeak

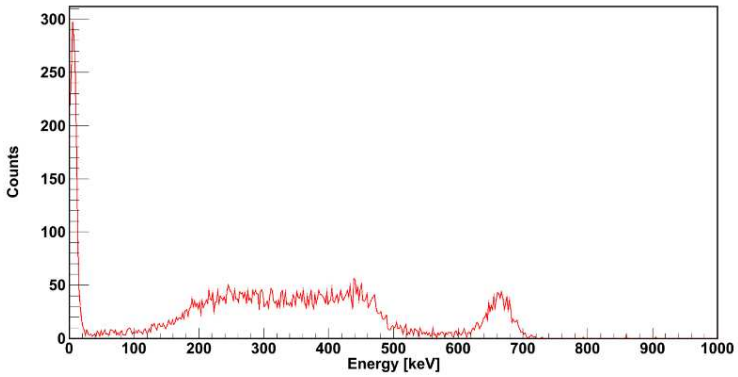

Figure 3: Calibrated spectrum for Cs-137 Source. Peak in the spectrum is the 662 keV photopeak

4. Applications

One application for CLYC is a handheld neutron and gamma ray detector. Current handheld detectors, such as those that use Helium-3 for neutron detection require complicated cooling systems. A handheld detector using CLYC would be much simpler to use. However, as with all handheld units, there must be batteries. In the case of CLYC, Li-Ion batteries are used. These batteries could capture some of the neutrons before they reach the detector, resulting in incorrect count rates. To test this, the batteries were placed in three positions around a CLYC crystal and exposed to a neutron source. In each of the positions, counts were recorded for 12 hours. The results of this test are shown in Table 1. When the batteries were placed between the crystal and the source, the neutron count rate dropped by a factor of 1.5. This suggests that the batteries could be a concern for the handheld neutron detector, but accurate modeling will be needed to verify these results.

Battery Position	Count Rate (cts/hr)
No Battery	2463
In Front	1390
Below	2572
Side	2517

Table 1: Neutron Count Rates for Various Battery Positions

5. Conclusions

The work presented here focuses around preparing to measure the proton response of CLYC. This new scintillating material can detect and distinguish ionizing radiation and thermal neutrons using pulse shape discrimination. The calibration using known sources was successful, and the same process will be performed when CLYC is taken to IBML for testing. The initial results for the curve fitting technique for pulse shape discrimination show promise that it could be useful. However, the process by which the parameters are calculated will need to become automated if the technique will be applied to a large enough set of waveforms. Finally, the testing with the batteries raises some concern about the handheld application for CLYC. Accurate modeling of the Li-Ion batteries will be needed to run simulations to test the results of this study. If the results are accurate, this attenuation will need to be compensated for in the final design of the instrument.

References

Glodo, J., Brys, W., Entine, G., Higgins, W., van Loef, E., Squillante, M., Shah, K., 2007. Cs_2LiYCl_6:Ce Neutron gamma detection system, in: Nuclear Science Symposium Conference Record, 2007. NSS '07. IEEE, pp. 959 –962.

Glodo, J., Higgins, W., van Loef, E., Shah, K., 2008. Scintillation Properties of 1 Inch Cs_2LiYCl_6:Ce Crystals. Nuclear Science, IEEE Transactions on 55, 1206 –1209.

Whistler turbulence forward cascade: Three-dimensional particle-in-cell simulations

Ouliang Chang

Department of Astronautical Engineering, University of Southern California, Los Angeles, California

S. Peter Gary

Los Alamos National Laboratory, Los Alamos, New Mexico

Joseph Wang

Department of Astronautical Engineering, University of Southern California, Los Angeles, California

Abstract

The first fully three-dimensional particle-in-cell (PIC) simulation of whistler turbulence in a magnetized, homogeneous, collisionless plasma has been carried out. An initial relatively isotropic spectrum of long-wavelength whistlers is imposed upon the system, with an initial electron $\beta = 0.10$. As in previous two-dimensional simulations of whistler turbulence, the three-dimensional system exhibits a forward cascade to shorter wavelengths and broadband, turbulent spectra with a wavevector anisotropy in the sense of stronger fluctuation energy at $k_\perp$ than at comparable $k_\parallel$ where the respective subscripts represent directions perpendicular and parallel to the background magnetic field $\mathbf{B}_o$. However, the three-dimensional (3D) simulations display quantitative differences with comparable two-dimensional (2D) computations. In the 3D runs, turbulence develops a stronger anisotropic cascade more rapidly than in 2D runs. Futhermore, reduced magnetic fluctuation spectra in 3D runs are less steep functions of perpendicular wavenumbers than those from 2D simulations. The much larger volume of perpendicular wavevector space in 3D appears to facilitate the transfer of fluctuation energy toward perpendicular directions.

Citation: Chang, O., P. S. Gary, and J. Wang (2011), Whistler turbulence forward cascade: Three-dimensional particle-in-cell simulations, Los Alamos Space Weather Summer School Reports 2011, pp. 5-12, LA-UR 12-00074, ISBN 978-0-9850208-1-1

Keywords: Whistler turbulence, Particle-In-Cell simulation

1. Introduction

Historically, the primary focus for the study of plasma turbulence in the solar wind has been on the inertial range at observed frequencies $f < 0.2$ Hz [e.g., *Horbury et al.*, 2005; *Matthaeus and Velli*, 2011]. In this regime, magnetic fluctuation energy spectra exhibit dependences on frequency of the form $|\delta\mathbf{B}(f)|^2 \sim (f)^{-\alpha_f}$ with $\alpha_f \simeq 5/3$ and a strong characteristic wavevector anisotropy with greater fluctuation energy at propagation quasi-perpendicular to $\mathbf{B}_o$, the average background magnetic field, than at quasi-parallel propagation. At a frequency near 0.2 Hz $< f <$ 0.5 Hz, measurements at 1 AU show a spectral break, a distinct change to spectra that are steeper than those of the inertial range [*Leamon et al.*, 1998; *Smith et al.*, 2006; *Alexandrova et al.*, 2008]. At observed frequencies above this break, magnetic spectra exhibit steeper power laws, i.e., with $2.0 < \alpha_f$ [*Behannon*, 1978; *Denskat et al.*, 1983; *Goldstein et al.*, 1994; *Lengyel-Frey et al.*, 1996; *Bale et al.*, 2005]. Recent analyses of data from the Cluster mission spacecraft have shown that magnetic spectra in the range 0.5 Hz $< f <$ 20 Hz scale with $2.6 < \alpha_f < 2.8$ [*Sahraoui et al.*, 2009, 2010; *Kiyani et al.*, 2009; *Alexandrova et al.*, 2009], and suggest that there is a second break with still more steeply decreasing spectra at 20 Hz $< f$. Some of these observations (*Chen et al.*, 2010; *Sahraoui et al.*, 2010)

Email addresses: ouliang@usc.edu (Ouliang Chang), pgary@lanl.gov (S. Peter Gary), josephjw@usc.edu (Joseph Wang)

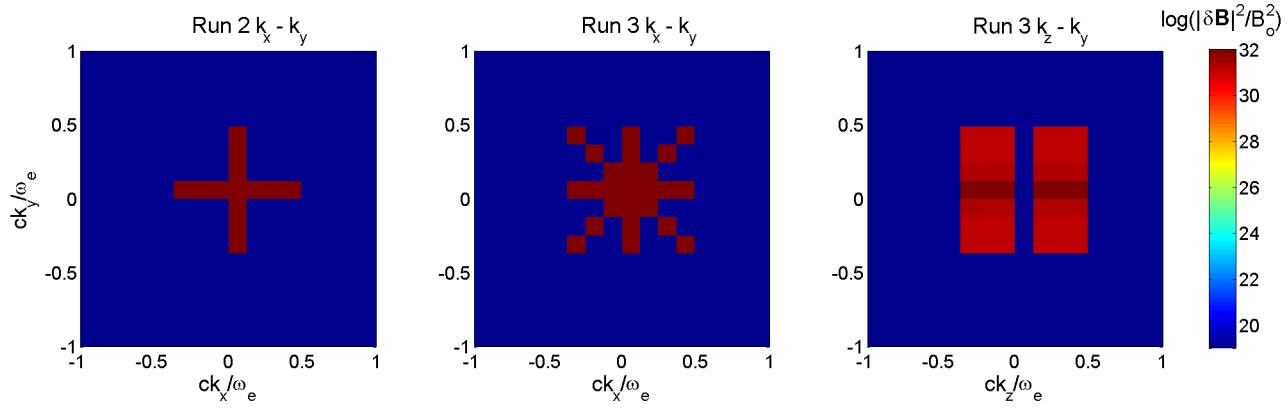

Figure 1: Two-dimensional reduced magnetic fluctuation energy spectra at $t = 0$: (left panel) Run 2 in the plane perpendicular to $\mathbf{B}_o$, (center panel) Run 3 in the plane perpendicular to $\mathbf{B}_o$, and (right panel) Run 3 in the k_y-k_z plane containing $\mathbf{B}_o$.

also demonstrated that this turbulence is anisotropic in the sense of having more fluctuation energy at propagation perpendicular to $\mathbf{B}_o$, where $\mathbf{B}_o$ denotes an average, uniform background magnetic field, than at propagation parallel or antiparallel to $\mathbf{B}_o$.

High frequency turbulence above the first spectral break is of small amplitude ($|\delta\mathbf{B}|^2 << B_o^2$), so that such turbulence is often described in terms of weakly interacting normal modes of the plasma with properties derived from linear dispersion theory. In this framework, there are two competing hypotheses as to the character of these fluctuations. One scenario is that this short-wavelength turbulence consists of kinetic Alfvén waves which propagate in directions quasi-perpendicular to $\mathbf{B}_o$ and at real frequencies $\omega_r < \Omega_p$, the proton cyclotron frequency. Both solar wind observations [*Leamon et al.*, 1998; *Bale et al.*, 2005; *Sahraoui et al.*, 2009, 2010] and gyrokinetic simulations [*Howes et al.*, 2008a, 2011; see also *Matthaeus et al.*, 2008, and *Howes et al.*, 2008c] of turbulence above the first break have been interpreted as consisting of kinetic Alfvén waves, although others have indicated that such fluctuations do not necessarily provide a complete description of short wavelength turbulence [*Gary and Smith*, 2009; *Podesta et al.*, 2010; *Chen et al.*, 2010]. A fluid model of kinetic Alfvén turbulence, which does not include kinetic plasma effects, yields magnetic fluctuation energy spectra which scale as $k_\perp^{-7/3}$, while inclusion of kinetic effects leads to still steeper spectra [*Howes et al.*, 2008b]. A recent three-dimensional gyrokinetic simulation of kinetic Alfvén turbulence has exhibited a $k_\perp^{-2.8}$ magnetic fluctuation spectrum [*Howes et al.*, 2011].

A second hypothesis is that whistler fluctuations at frequencies below the electron cyclotron frequency contribute to short-wavelength turbulence. Whistlers are often observed in the solar wind [*Beinroth and Neubauer*, 1981; *Lengyel-Frey et al.*, 1996]. Simulations of whistler turbulence using three-dimensional electron magnetohydrodynamic (EMHD) fluid models [*Biskamp et al.*, 1999; *Cho and Lazarian*, 2004, 2009; *Shaikh*, 2009] typically show a forward cascade to steep magnetic spectra with $k^{-7/3}$, and anisotropies similar to those of the inertial range with greater fluctuation energy at quasi-perpendicular propagation. Two-dimensional particle-in-cell (PIC) simulations of whistler turbulence [*Gary et al.*, 2008, 2010; *Saito et al.*, 2008, 2010; *Svidzinski et al.*, 2009], which include full kinetic effects such as Landau and cyclotron wave-particle interactions, also demonstrate forward cascades to anisotropic magnetic spectra with very steep wavenumber dependences (e.g., $k_\perp^{-4}$). Here we describe the first PIC simulations to examine the forward cascade of whistler turbulence in a fully three-dimensional plasma model.

Our simulation results are derived from a three-dimensional electromagentic particle-in-cell code 3D EMPIC described by *Wang et al.* [1995]. In this code, plasma particles are pushed using a standard relativistic particle algorithm; currents are deposited using a rigorous charge conservation scheme [*Villasenor and Buneman*, 1992]; and the self-consistent electromagnetic field is solved using a local finite difference time domain solution to the full Maxwell's equations. This code was recently modified and updated for this work. Specifically, the parallel computing part of the code has been optimized for hybrid parallel implementation to perform multithreading on clusters with multicore-processors. Space-filling curves are used in sorting particle array to preserve nearest-neighbor

cells' proximity in memory. Such spatial proximity would enhance data locality, reduce cache miss, and thus further speed up the code. Our 3D simulations are performed at USC's HPC and NASA's Pleiades supercomputer systems. The upgraded 3D EMPIC code scales extremely well, with over 96% parallel efficiency on 2048 cores. The typical wall time of 3D runs is around 16 ~ 17 hours.

We denote the jth species plasma frequency as $\omega_j \equiv \sqrt{4\pi n_j e_j^2/m_j}$, the jth species cyclotron frequency as $\Omega_j \equiv e_j B_o/m_j c$, and $\beta_{\|j} \equiv 8\pi n_j k_B T_{\|j}/B_o^2$. We consider an electron-proton plasma where subscript e denotes electrons and p stands for protons.

Here "three-dimensional" means that the simulation includes variations in three spatial dimensions, as well as calculating the full three-dimensional velocity space response of each ion and electron superparticle. The plasma is homogeneous with periodic boundary conditions. The uniform background magnetic field is $\mathbf{B}_o = \hat{\mathbf{z}} B_o$ so that the subscripts z and $\|$ represent the same direction. Thus $\mathbf{k} = \hat{\mathbf{x}} k_x + \hat{\mathbf{y}} k_y + \hat{\mathbf{z}} k_\|$ and $k_\perp = \sqrt{k_x^2 + k_y^2}$. We define two-dimensional reduced energy spectra by summation over the third Cartesian wavevector component, e.g.,

$$|\delta\mathbf{B}(k_x, k_y)|^2 \equiv \Sigma_{k_z} |\delta\mathbf{B}(\mathbf{k})|^2 \quad .$$

Similarly, one-dimensional reduced spectra for $k_\|$ are obtained by summation over the two perpendicular wavevector components:

$$|\delta\mathbf{B}(k_\|)|^2 \equiv \Sigma_{k_x, k_y} |\delta\mathbf{B}(\mathbf{k})|^2 \quad .$$

In contrast, the one-dimensional reduced spectra for $k_\perp$ are obtained by summing the energy over both $k_\|$ and concentric annular regions in k_x-k_y space. The total fluctuating magnetic energy density is obtained by summing over all simulation wavevectors:

$$|\delta\mathbf{B}|^2 \equiv \Sigma_{\mathbf{k}} |\delta\mathbf{B}(\mathbf{k})|^2$$

and the spectral anisotropy angle θ_B is defined via

$$\tan^2 \theta_B \equiv \frac{\Sigma_{\mathbf{k}}\, k_\perp^2 |\delta\mathbf{B}(\mathbf{k})|^2}{\Sigma_{\mathbf{k}}\, k_\|^2 |\delta\mathbf{B}(\mathbf{k})|^2} \quad .$$

An isotropic spectrum corresponds to $\tan^2 \theta_B$ =1.0. In the evaluation of each of these quantities, the wavenumber range of the summations is over the cascaded fluctuations; i.e., $0.55 \le |kc/\omega_e| \le 3.0$.

2. Simulations

This section describes results from three PIC simulations of the forward cascade of freely decaying whistler turbulence. For all three runs, as in *Gary et al.* [2008] and *Saito et al.* [2008], the grid spacing is $\Delta = 0.10 c/\omega_e$, where c/ω_e is the electron inertial length, the time step is $\delta t\ \omega_e = 0.05$ and the number of superparticles per cell is 64. The system has a spatial length of $51.2 c/\omega_e$ in each direction. For these parameters, the fundamental mode of all three simulations has wavenumber $kc/\omega_e = 0.1227$, and short wavelength fluctuations should be resolved up to the component wavenumber of $k_\| c/\omega = k_\perp c/\omega_e = 4$. As in the two-dimensional simulations of *Saito et al.* [2008] and *Gary et al.* [2008, 2010], the initial physical dimensionless parameters are $m_p/m_e = 1836$, $T_e/T_p = 1.0$, $\beta_e = 0.10$, and $\omega_e^2/\Omega_e^2 = 5.0$.

We impose a three-dimensional spectrum of right-hand polarized whistler waves at $t = 0$. Initial wavenumbers parallel to $\mathbf{B}_o$ are $k_\| c/\omega_e = \pm\, 0.1227, \pm\, 0.2454$, and $\pm\, 0.3682$, whereas initial perpendicular wavenumbers are the six same values and $k_\perp c/\omega_e = 0$. Different runs have different number (N) of modes imposed in the system, however, the initial total fluctuating magnetic field energy density is the same for all three runs: $\sum_{n=1}^{N} |\delta\mathbf{B}_n(t=0)|^2/B_o^2 = 0.10$. The method of loading such an initial spectrum is described in *Saito et al.* [2008]. The frequencies and relationships among the field components are derived from the linear dispersion equation for magnetosonic-whistler fluctuations in a collisionless plasma, but the subsequent evolution of the fields and particles are computed using the fully nonlinear particle-in-cell simulation code.

Run 1 is a two-dimensional simulation with an initial spectrum similar to the corresponding runs of *Gary et al.* [2008] and *Saito et al.* [2008]. The domain size is 512×512 cells, which is equivalent to $51.2 c/\omega_e \times 51.2 c/\omega_e$. In

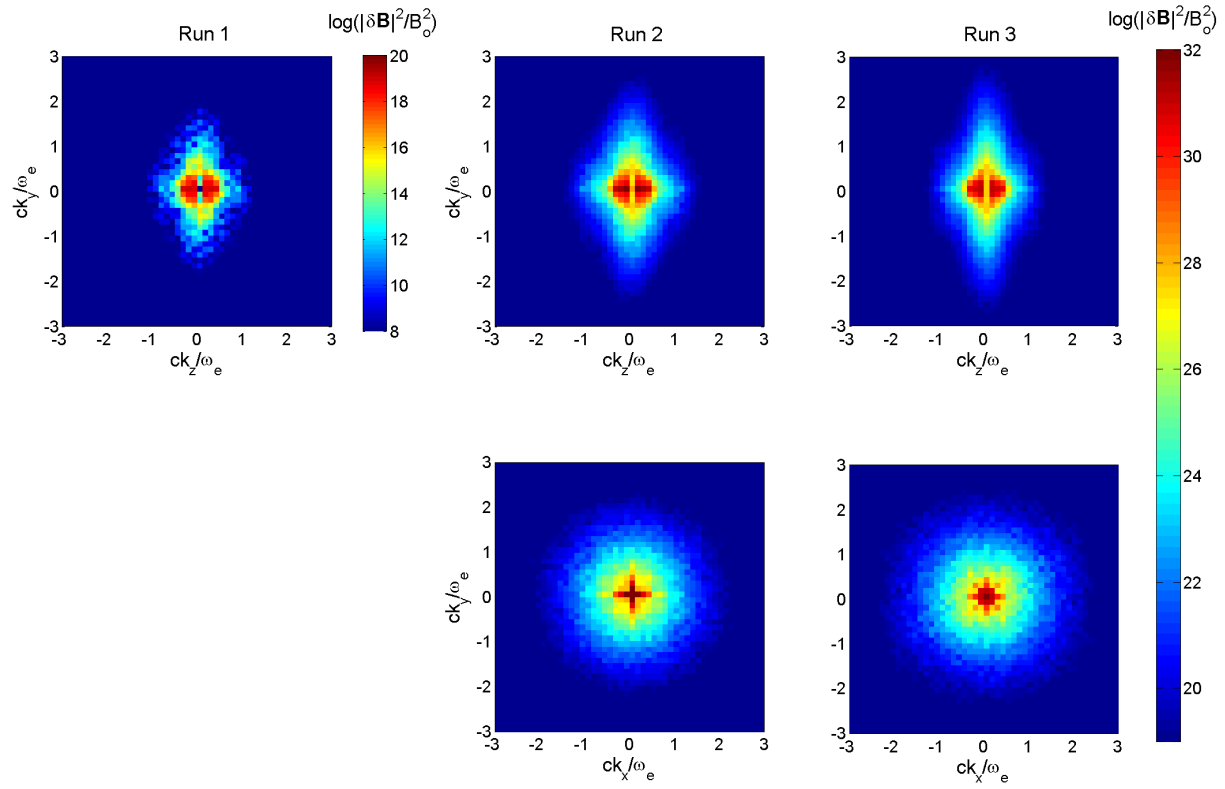

Figure 2: Two-dimensional reduced magnetic fluctuation energy spectra at $|\Omega_e|t$ = 447 from Run 1 (left panel), Run 2 (center panels) and Run 3 (right panels). The upper row of panels represents spectra in the k_y-k_z plane, whereas the bottom row of panels represents spectra in the plane perpendicular to $\mathbf{B}_o$.

this case, 42 modes are present in the y-z plane of the initial whistler spectrum. Runs 2 and 3 are three-dimensional simulations in which the system has a domain size of $512 \times 512 \times 512$ cells and spatial dimensions $L_x = L_y = L_z = 51.2c/\omega_e$. The only difference between these two runs is in the initial spectra. Run 2 has 42 modes in the y-z plane and 36 modes in the x-z plane (omitting the 6 modes at $k_\perp = 0$), whereas Run 3 has the same 78 modes as Run 2, but an additional 72 modes corresponding to a rotation of the Run 2 modes through an angle of 45^o about the z-axis. Figure 1 illustrates the distribution of the initial modes for the two three-dimensional cases. All three runs are computed to a final time of $|\Omega_e|t$ =447. The total particle plus fluctuating field energy of the system is conserved to within 0.6% between $t = 0$ and the final time.

Figure 2 shows two-dimensional reduced magnetic energy spectra from the three simulations at the final time. As in the two dimensional Run 1, the imposition of an initial spectrum of relatively long-wavelength whistlers in the three-dimensional runs leads to a forward cascade to shorter wavelengths and the development of a broadband, turbulent spectrum. The late-time spectrum in the k_x-k_y plane perpendicular to $\mathbf{B}_o$ is approximately gyrotropic, which is a consistency check on our homogeneous plasma simulation with initial conditions which are symmetric between x and y. The late-time reduced spectra in the two planes (k_x-k_z, k_y-k_z) containing $\mathbf{B}_o$ in all three runs show, just as in the two-dimensional PIC simulations of whistler turbulence [*Gary et al.*, 2008, 2010; *Saito et al.*, 2008, 2010], that the forward cascade is anisotropic, preferentially transfering energy to fluctuations with wavevectors quasi-perpendicular, rather than quasi-parallel, to $\mathbf{B}_o$.

The reduced magnetic k_y spectrum from the two-dimensional Run 1 at $|\Omega_e|t$ = 447 has a power-law dependence of approximately k_y^{-4}, similar to the $k_y^{-4.5}$ late-time results for the two-dimensional simulations with $\epsilon = 0.10$ and

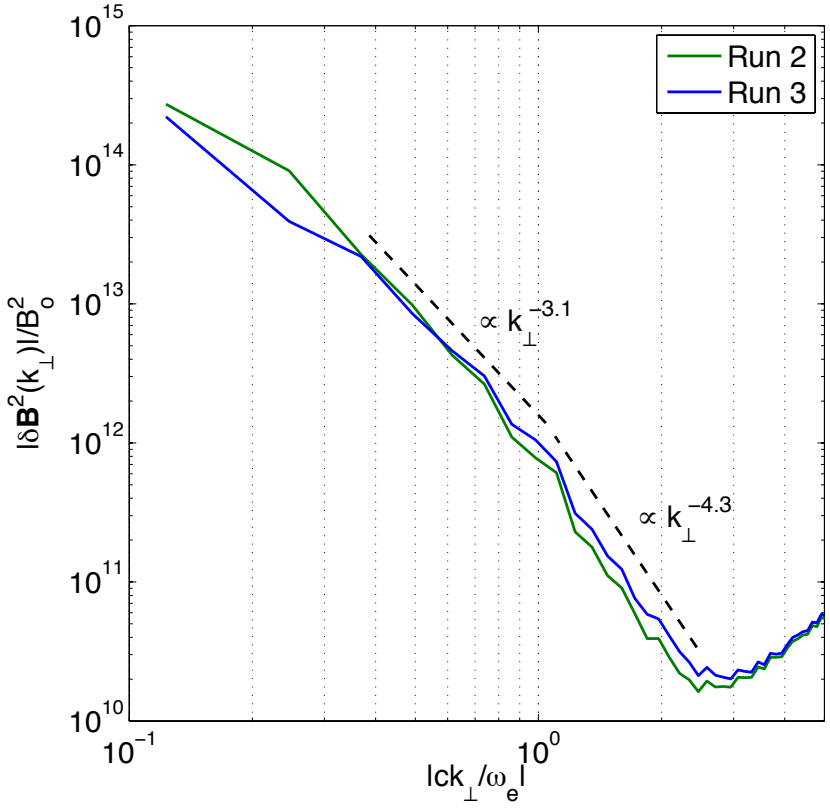

Figure 3: Reduced $k_\perp$ magnetic fluctuation energy spectra at $|\Omega_e|t = 447$ from Run 2 (red line) and Run 3 (blue line). The dashed lines represent power law functions as labeled for comparison against the simulation results.

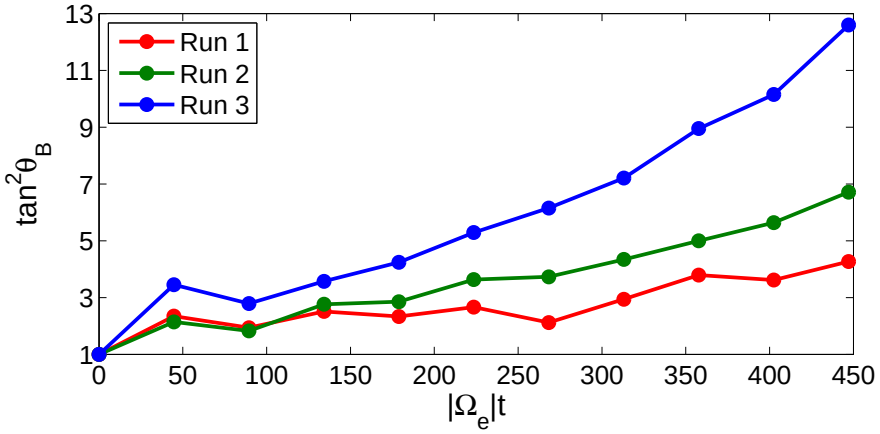

Figure 4: Time histories of the spectral anisotropy factor $\tan^2\theta_B$ from the two-dimensional Run 1 (red line) and the three-dimensional Run 2 (blue line) and Run 3 (green line) simulations. Evaluations here are taken on spectra over $0.65 \leq kc/\omega_e \leq 3.0$.

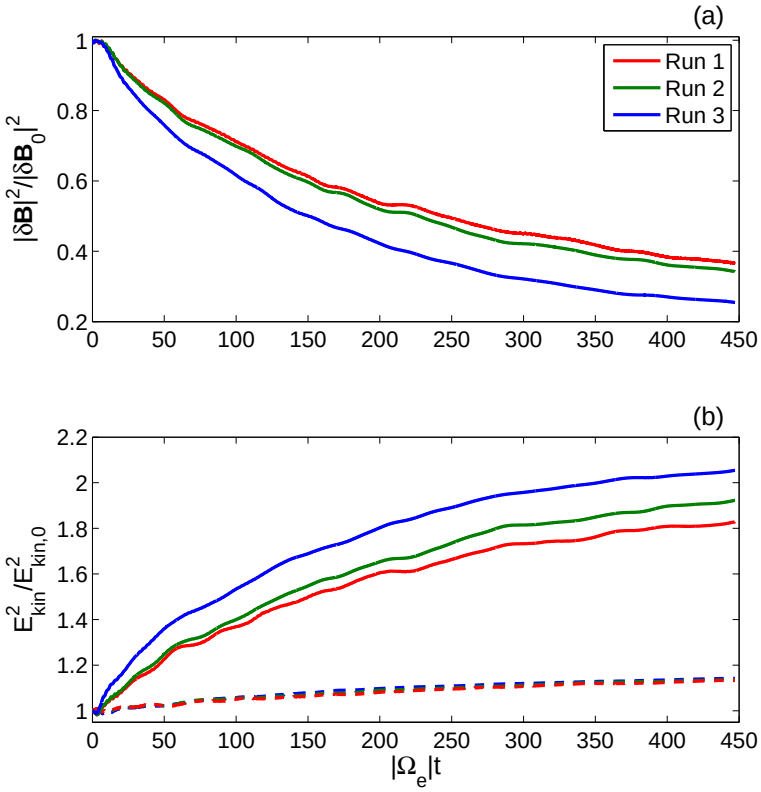

Figure 5: Time histories of the (a) total fluctuating magnetic energy density and (b) the parallel (solid lines) and perpendicular (dashed lines) components of the total electron kinetic energy as functions of time. Here the red lines represent the two-dimensional Run 1 whereas the green and blue lines represent the three-dimensional Runs 2 and 3, respectively.

initial $\beta_e = 0.10$ of *Gary et al.* [2008] and *Saito et al.* [2008]. Figure 3 illustrates the $k_\perp$ reduced spectra from the three-dimensional Run 2 and Run 3. The results for the two runs are very similar, indicating that the late-time spectra are relatively independent of the detailed choice of initial fluctuations. The dashed lines, drawn to guide the eye, suggest a power law dependence of $k_\perp^{-3}$ at relatively long wavelengths ($0.2 < k_\perp c/\omega_e < 1$) and a steeper wavenumber dependence of $k_\perp^{-4}$ at shorter wavelengths ($1 < k_\perp c/\omega_e$). The upturn in the spectra at $k_\perp c/\Omega_e \simeq 2.5$ corresponds to the noise level of the simulation. The suggestion of two distinct power-law regimes of the turbulence is similar to the prediction of *Meyrand and Galtier* [2010] who used an EMHD model with isotropic fluctuations to derive a $k^{-11/3}$ magnetic fluctuation spectrum at $1 < kc/\omega_e$. High-frequency turbulent spectra with breaks near the inverse electron inertial length have also been reported in the solar wind observations of *Sahraoui et al.* [2009, 2010] and *Alexandrova et al.* [2009].

Figure 4 compares the spectral anisotropies $\tan^2\theta_B$ of the three runs as functions of time. The results of the two-dimensional Run 1 are very similar to that of Run I from *Saito et al.* [2008], with $\tan^2\theta_B \sim 4$ at $|\Omega_e|t \simeq 400$. Both three-dimensional runs exhibit stronger anisotropies, with Run 2 reaching $\tan^2\theta_B \simeq 6$ and Run 3 attaining $\tan^2\theta_B > 10$ at late times. Our interpretation of these results is that the much larger number of quasi-perpendicular modes available in the three-dimensional cases allows the nonlinear wave-wave interactions and perpendicular cascades to proceed much more efficiently than in two dimensions. The successively increasing number of modes with $k_\perp$ components among these three runs implies more channels for perpendicular cascading and therefore a successively faster rate of such energy transfer for the fluctuations. Limits on our computational resources prevent us from continuing to move toward more dense modes in wavevector space, but the trend of these three runs indicates that such a condition should

correspond to a highly anisotropic late-time condition with $\tan^2\theta_B >> 1$.

Figure 5(a) shows the total fluctuating magnetic field energy density as a function of time. Results of all three runs are qualitatively similar, demonstrating a gradual decrease of the total fluctuating magnetic field energy density. However, the three-dimensional simulations exhibit faster rates of fluctuation energy dissipation than the two-dimensional Run 1. Figure 5(b) shows that electrons have greater parallel kinetic energy gains in the three-dimensional runs than in the two-dimensional Run 1. The perpendicular energy gain of electrons is much weaker in all three runs, and there is no significant difference in this energy gain among the three cases.

Fig. 7 of *Saito et al.* [2008] shows that, at $k_\parallel c/\omega_e < 1$, the Landau resonance at oblique propagation is a stronger mechanism for whistler damping than the cyclotron resonance. Figure 4 shows that three-dimensional whistler turbulence (Runs 2 and 3) is more efficient at transferring fluctuation energy to oblique propagation than two-dimensional such turbulence (Run 1), implying that, at such long wavelengths, 3D whistler turbulence is more efficient at dissipation than its two-dimensional counterpart. This provides a plausible explanation for the more rapid decrease of the fluctuating energy in the 3D simulations illustrated in Figure 5(a).

3. Conclusions

We have carried out the first fully three-dimensional particle-in-cell simulations of whistler turbulence in a homogeneous collisionless plasma with a uniform background magnetic field $\mathbf{B}_o$. We imposed an initial spectrum of relatively long-wavelength whistler fluctuations and computed the free decay of these modes to a broadband shorter wavelength regime of turbulence. This cascade yielded transfer of fluctuation energy to wavevectors preferentially quasi-perpendicular to $\mathbf{B}_o$. Both the forward cascade and its consequent wavevector anisotropy are qualitatively similar to previous results obtained from two-dimensional PIC simulations of whistler turbulence; quantitatively, however, the three-dimensional anisotropy develops faster and to a larger value than that in two-dimensional simulations. Furthermore, the more modes that are used as initial conditions, the more rapid the cascade and the more strongly anisotropic the turbulence becomes.

The reduced magnetic fluctuation energy spectrum of our two-dimensional simulation shows an approximately k_y^{-4} dependence at $k_\perp c/\omega_e < 1$, similar to the steep power-law behavior exhibited in earlier such simulations [*Saito et al.*, 2008, 2010]. In contrast, the three-dimensional simulations of Runs 2 and 3 show a less steep one-dimensional reduced magnetic spectral power-law dependence of approximately $k_y^{-2.8}$ at $k_\perp c/\omega_e < 1$. Further three-dimensional simulations of whistler turbulence at different values of β_e and initial fluctuation amplitude must be carried out before further conclusions concerning whistler turbulence are reached.

Solar wind observations typically show $\beta_e \sim 1$, at which values electron Landau damping is strong and competes with wave-wave cascade processes. We have here used $\beta_e = 0.10$ to reduce Landau damping and to permit our simulations to isolate the consequences of wave-wave interactions. A complete study of whistler turbulence should address the high-β regime as well, but is beyond the purview of this work.

References

Alexandrova, O., V. Carbone, P. Veltri, and L. Sorriso-Valvo (2008), Small-scale energy cascade of the solar wind turbulence, *Astrophys. J.674*, 1153.

Alexandrova, O., J. Saur, C. Lacombe, A. Mangeney, J. Mitchell, S. J. Schwartz, and P. Robert (2009), Universality of solar wind turbulent spectrum from MHD to electron scales, *Phys. Rev. Lett.103*, 165003.

Bale, S. D., P. J. Kellogg, F. S. Mozer, T. S. Horbury, and H. Reme (2005), Measurement of the electric fluctuation spectrum of magnetohydrodynamic turbulence, *Phys. Rev. Lett.94*, 215002.

Behannon, K. W. (1978), Heliocentric distance dependence of the interplanetary magnetic field, *Revs. Geophys.*, *16*, 125.

Beinroth, H. J., and F. M. Neubauer (1981), Properties of whistler mode waves between 0.3 and 1.0 AU from Helios observations, *J. Geophys. Res.86*, 7755.

Biskamp, D., E. Schwarz, A. Zeiler, A. Celani, and J. F. Drake (1999), Electron magnetohydrodynamic turbulence, *Phys. Plasmas*, *6*, 751.

Cho, J., and A. Lazarian (2004), The anisotropy of electron magnetohydrodynamic turbulence, *Astrophys. J.615*, L41.

Cho, J., and A. Lazarian (2009), Simulations of electron magnetohydrodynamic turbulence, *Astrophys. J.701*, 236.

Chen, C. H. K., T. S. Horbury, A. A. Schekochihin, R. T. Wicks, O. Alexandrova, and J. Mitchell (2010), Anisotropy of solar wind turbulence in the dissipation range, *Phys. Rev. Lett.104*, 255002.

Denskat, K. U., H. J. Beinroth, and F. M. Neubauer (1983), Interplanetary magnetic field power spectra with frequencies from 2.4 x 10^{-5} Hz to 470 Hz from HELIOS- observations during solar minimum conditions, *J. Geophys.*, *54*, 60.

Gary, S. P., and C. W. Smith (2009), Short-wavelength turbulence in the solar wind: Linear theory of whistler and kinetic Alfvén fluctuations, *J. Geophys. Res.114*, A12105, doi:10.1029/2009JA014525.

Gary, S. P., S. Saito, and H. Li (2008), Cascade of whistler turbulence: Particle-in-cell simulations, *Geophys. Res. Lett.35*, L02104, doi:10.1029/2007GL032327.

Gary, S. P., S. Saito, and Y. Narita (2010), Whistler turbulence wavevector anisotropies: Particle-in-cell simulations, *Astrophys. J.716*, 1332.

Goldstein, M. L., D. A. Roberts, and C. A. Fitch (1994), Properties of the fluctuating magnetic helicity in the inertial and dissipation ranges of solar wind turbulence, *J. Geophys. Res.99*, 11,519.

Horbury, T. S., M. A. Forman, and S. Oughton (2005), Spacecraft observations of solar wind turbulence: An overview, *Plasma Phys. Control. Fusion*, *47*, B703.

Howes, G. G., W. Dorland, S. C. Cowley, G. W. Hammett, E. Quataert, A. A. Schekochihin, and T. Tatsuno (2008a), Kinetic simulations of magnetized turbulence in astrophysical plasmas, *Phys. Rev. Lett.100*, 065004.

Howes, G. G., S. C. Cowley, W. Dorland, G. W. Hammett, E. Quataert, and A. A. Schekochihin (2008b), A model of turbulence in magnetized plasmas: Implications for the dissipation range in the solar wind, *J. Geophys. Res.*, *113*, A05103.

Howes, G. G., S. C. Cowley, W. Dorland, G. W. Hammett, E. Quataert, A. A. Schekochihin, and T. Tatsuno (2008c), Reply, *Phys. Rev. Lett.101*, 149502.

Howes, G. G., J. M. TenBarge, W. Dorland, E. Quataert, A. A. Schekochihin, R. Numata, and T. Tatsuno (2011), Gyrokinetic simulations of solar wind turbulence from ion to electron scales, *Phys. Rev. Lett.107*, 035004.

Kiyani, K. H., S. C. Chapman, Yu. V. Khotyaintsev, M. W. Dunlop, and F. Sahraoui (2009), Global scale-invariant dissipation in collisionless plasma turbulence, *Phys. Rev. Lett.103*, 075006.

Leamon, R. J., C. W. Smith, N. F. Ness, W. H. Matthaeus, and H. K. Wong (1998), Observational constraints on the dynamics of the interplanetary magnetic field dissipation range, *J. Geophys. Res.103*, 4775.

Lengyel-Frey, D., R. A. Hess, R. J. MacDowall, R. G. Stone, N. Lin, A. Balogh, and R. Forsyth (1996), Ulysses observations of whistler waves at interplanetary shocks and in the solar wind, *J. Geophys. Res.101*, 27,555.

Matthaeus, W. H., S. Servidio, and P. Dmitruk (2008), Comment on "Kinetic simulations of magnetized turbulence in astrophysical plasmas," *Phys. Rev. Lett.101*, 149501.

Matthaeus, W. H., and M. Velli (2011), Who needs turbulence? A review of turbulence effects in the heliosphere and on the fundamental process of reconnection, *Space Sci. Revs.*, doi 10.1007/s11214-011-9793-9.

Meyrand, R., and S. Galtier (2010), A universal law for solar-wind turbulence at electron scales, *Astrophys. J.721*, 1421.

Podesta, J. J., J. E. Borovsky, and S. P. Gary (2010), A kinetic Alfvén wave cascade subject to collisionless damping cannot reach electron scales in the solar wind at 1 AU, *Astrophys. J.712*, 685.

Sahraoui, F., M. L. Goldstein, P. Robert, and Yu. V. Khotyaintsev (2009), Evidence of a cascade and dissipation of solar-wind turbulence at the electron gyroscale, *Phys. Rev. Lett.102*, 231102.

Sahraoui, F., M. L. Goldstein, G. Belmont, P. Canu, and L. Rezeau (2010), Three dimensional anisotropic k spectra of turbulence at subproton scales in the solar wind, *Phys. Rev. Lett.105*, 131101.

Saito, S., S. P. Gary, H. Li, and Y. Narita (2008), Whistler turbulence: Particle-in-cell simulations, *Phys. Plasmas*, *15*, 102305.

Saito, S., S. P. Gary, and Y. Narita (2010), Wavenumber spectrum of whistler turbulence: Particle-in-cell simulation, *Phys. Plasmas*, *17*, 122316.

Shaikh, D. (2009), Whistler wave cascades in solar wind plasma, *Mon. Not. R. Astron. Soc.*, *395*, 2292.

Smith, C. W., K. Hamilton, B. J. Vasquez, and R. J. Leamon (2006), Dependence of the dissipation range spectrum of interplanetary magnetic fluctuations on the rate of energy cascade, *Astrophys. J.645*, L85.

Svidzinski, V. A., H. Li, H. A. Rose, B. J. Albright, and K. J. Bowers (2009), Particle in cell simulations of fast magnetosonic wave turbulence in the ion cyclotron frequency range, *Phys. Plasmas*, *16*, 122310.

Villasenor, J., and O. Buneman (1992), Rigorous charge conservation for local electromagnetic field solvers, *Comput. Phys. Commun.*, *69*, 306.

Wang, J., P. Liewer, and V. Decyk (1995), 3D electromagnetic plasma particle simulations on a MIMD parallel computer, *Comput. Phys. Commun.*, *87*, 35.

Sensitivity Analysis for L^*

Justin Elfritz

Department of Physics, West Virginia University

Jonathan Niehof

Los Alamos National Laboratory

Abstract

A sensitivity analysis for L^*, a variation of the third adiabatic invariant, is being performed. This report will address the importance of L^* in the magnetosphere, and why framing the physics in terms of L^* is appropriate. The physical quantities on which L^* depends: Kp (for our simplified magnetic field model), spatial location, and particle pitch angle, will also be discussed along with a planned re-casting of the problem into a slightly different parameter space defined by Kp, the integral invariant I, Earth's dipole tilt, and Earth's rotation phase. L^* data calculated using the LanlGeoMag package is presented to illustrate one-dimensional dependence of L^* on I, spatial location, and Kp. Mathematical fits & correlations of potentially useful forms will be shown. A zeroth-order approximation that can reduce system dimensionality will also be discussed. A discussion of the future direction of this project will follow.

Citation: Elfritz, J. and J. Niehof (2011), Sensitivity Analysis for L*, Los Alamos Space Weather Summer School Reports 2011, pp. 13–18, LA-UR 12-00074, ISBN 978-0-9850208-1-1

Keywords: L^*, Drift Shell, Adiabatic Invariant, Radiation Belts, Magnetosphere

1. Introduction to L^*

L^* represents the third adiabatic invariant, which is associated with the drift motion charged particles experience in spatially inhomogeneous magnetic fields. In Earth's magnetosphere, field gradients and curvature of field lines produce this drift motion. Conserving L^* implies a fixed magnetic field topology on timescales comparable to a particles drift period, which is often a poor approximation since the driver of the non-dipolar features in the magnetic field, the solar wind, can change dramatically over a few minutes, while drift periods are typically measured in hours. L^* was by introduced in Roederer (1970), defined by the magnetic flux Φ enclosed by a particle drift shell, given the field $\vec{B}$ which closes at the high-latitude footpoints.

$$\Phi = \oint \vec{B} \cdot d\vec{S} \tag{1}$$

The definition of L^* follows as

$$L^* = \frac{2\pi M}{\Phi R_E} \tag{2}$$

where M is Earth's magnetic moment, and R_E is the average equatorial radius of Earth. L^* may be interpreted as the equatorial L-shell a particle will be on if all external, non-dipolar field components are adiabatically turned off. During quiet times, L^* may be approximated by the McIlwain L parameter, which is calculated under the assumption of a purely dipolar field. An accurate approximation to L^* is particularly important for understanding radial diffusion in the inner magnetosphere. Diffusion equations are expressed in phase space as functions of μ, K, and L^*, the three adiabatic

Email addresses: jelfritz@mix.wvu.edu (Justin Elfritz), jniehof@lanl.gov (Jonathan Niehof)

invariants. Radial diffusion in phase space, important in the radiation belts, is described in Green and Kivelson (2004) by

$$\frac{\partial f(\mu, K, L^*)}{\partial t} = \left(\frac{\partial D}{\partial L^*} - \frac{2D}{L^*}\right)\frac{\partial f}{\partial L^*} + D\frac{\partial^2 f}{\partial L^{*2}} \tag{3}$$

which shows that phase space density f can depend explicity on L^*, and implicitly through the form of D, which is a diffusion coefficient. Therefore understanding fluxes, transport, and acceleration mechanisms in the radiation belts requires an accurate global knowledge of L^*, as well as how diffusion coefficients are affected by external drivers. D is typically considered to obey a power law, as in Schulz and Lanzerotti (1974), scaled by a coefficient that may depend on these external drivers. In order to use the diffusion equation (3), it is necessary to convert flux measurements from spacecraft into corresponding phase space densities given in terms of the three adiabatic invariants,

$$j(\alpha, E, \vec{x}, t) \Rightarrow f(\mu, K, L^*) \tag{4}$$

described in detail by Green and Kivelson (2004). Here j is the flux calculated from raw instrument data, α is pitch angle, E is particle energy, $\vec{x}$ is spatial location, and t is time. This conversion has a computational bottleneck at the L^* calculation, because calculating L^* requires tracing an entire drift shell, whereas only a single field line must be traced to calculate L. During quiet periods in the magnetosphere, and for regions where Earth's dipole dominates the local field, L may be a good approximation. Otherwise, accurately determining particle motion requires accurate L^* calculations. This report outlines the early stages in sensitivity analysis for L^*, the aim of which is to develop an analytic form that will allow for quick calculations of L^* with acceptable error. L^* will depend on solar wind parameters through their influence the global magnetic field configuration. L^* will also depend on the particle pitch angle α, or equivalently the integral invariant K, or I. L^* will also depend explicitly on position $\vec{x}$ and time t, since seasonal and diurnal variations of Earth's rotation must be accounted for. Note that the $\vec{x}, t$ dependence can also be expressed in terms of ψ, ϕ.

2. Approach

This L^* study uses the Tsyganenko (1989) magnetic field model, which is parameterized solely by the Kp index. In response to increased Kp, the T89 field will produce a compression of dayside field lines while stretching the nightside field lines tailward. This feature causes drift shells to contract inward (higher Kp) or expand (lower Kp), which causes a particle at a given location to occupy a drift shell partially defined by the Kp index. L^* calculations were performed using LanlGeoMag over a range of spatial locations, pitch angles, and Kp indices, all at a fixed time t corresponding to midnight of the summer solstice 2010. 12 pitch angles ranging from 8° to 90° were used, which omits particles in or near the pitch angle loss cone. Kp values from 0 to 5, covering the low to moderate activity regime, were also used. L^* is calculated for all combinations of α and Kp on a 3-dimensional spatial grid shaped like a cylindrical shell with the axis of symmetry along Z_{GSM}. L^* calculations are performed at 21 Z_{GSM} coordinates in the range $[-3R_E, 3R_E]$. At each constant Z_{GSM}, L^* is calculated at 16 radial distances $R = \sqrt{X_{GSM}^2 + Y_{GSM}^2}$ in the range $[4R_E, 8R_E]$, and 20 X_{GSM}, Y_{GSM} coodinates at each R. Since these calculations are performed at fixed dipole tilt ψ and rotation phase ϕ, this yields a characterization of the dependence of L^* on I and Kp. This is the first stage in our attempt to cast the problem in the 4-dimensional parameter space defined by I, Kp, ψ, ϕ.

3. Results

In Figure 1, data illustrating the dependence of $L^*(I, Kp)$ is presented for noon, dawn, dusk, and midnight at $R = 4R_E$ at $Z_{GSM} = 0R_E$. Solid lines indicate $L^*(I)$ calculations at constant Kp using LanlGeoMag. Dashed lines represent quadratic fits to the $L^*(I)$ data, and assume the form

$$L^*(I) = c_2(Kp)I^2 + c_1(Kp)I + c_0(Kp) \tag{5}$$

An important feature of Fig.1 is the weak dependence that $L^*(I)$ displays for a given Kp, which is to say that for particles at $R = 4R_E$, the entire pitch angle distribution at a given $\vec{x}$ has roughly the same L^*. This weak dependence

is especially apparent near dawn and dusk where $L^* \approx L$ during quiet times, but even at noon and midnight the deviation from the mean is small. Therefore, ignoring temporal effects associated with diurnal and seasonal variations, L^* may be approximated to lowest order as a function only of Kp, provided an analytic form for the coefficients $c_2(Kp), c_1(Kp), c_0(Kp)$ which can be obtained numerically. This low order approximation suggests a simple mean of L^* values over the range of corresponding I, assuming an isotropic I distribution. If an alternative I distribution is known, a weighted mean will be more appropriate. Denote the I-averaged L^* value as $\langle L^* \rangle$, i.e.,

$$L^*(I, Kp) \approx \langle L^*(Kp) \rangle = \langle L^* \rangle \tag{6}$$

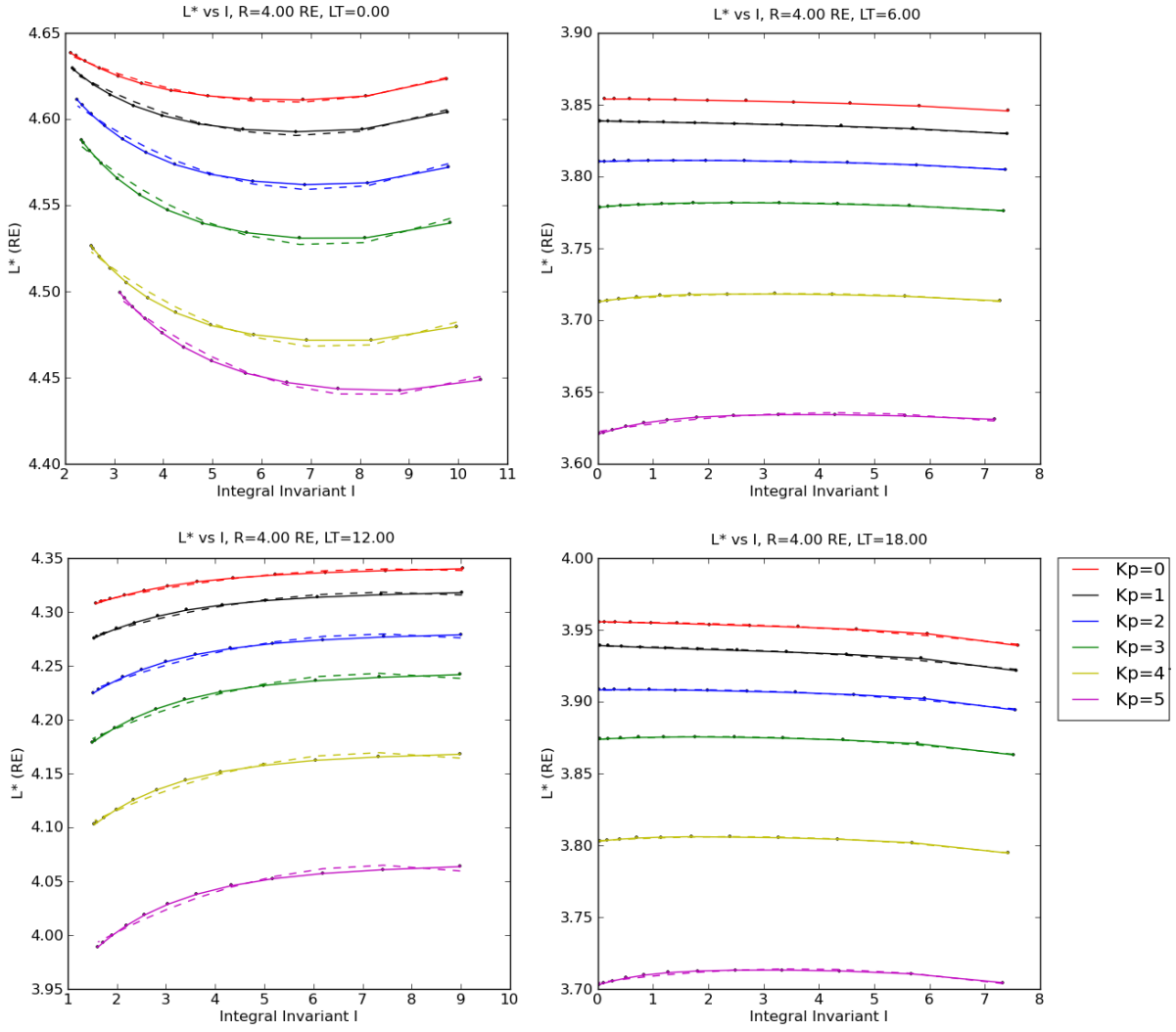

Figure 1: Figure 1. $L^*(I, Kp)$ is shown for a range of α, Kp, at 4 cardinal locations at $4R_E$, with $Z_{GSM} = 0R_E$. The dependence of L^* on Kp dominates over the I dependence, suggesting a low order approximation to the I dependence. This approximation has larger errors along the noon-midnight meridian.

Figure 2 illustrates what numerical error may result from this zeroth order approximation for $Kp = 1, 2, 3, 4$. The colorbar shows the variance in L^* normalized to $\langle L^* \rangle$ for each spatial bin, and white pixels indicate a bin where the

L^* calculation did not complete. It is worth noting that the normalized % variance does not exceed $\approx 2\%$ inside of geosynchronous orbit, implying that any drift shell that intersects a given point in space, out to roughly $R = 5R_E$ and near $Z_{GSM} = 0R_E$ can have any arbitrary pitch angle distribution, yet the particles will all share an approximately common L^* value, given a constant Kp. For this to be valid, we must also assume that the L^* dependence on position $\vec{x}$ and time t is known, which can be parameterized by the dipole tilt angle ψ and Earth's rotation phase ϕ.

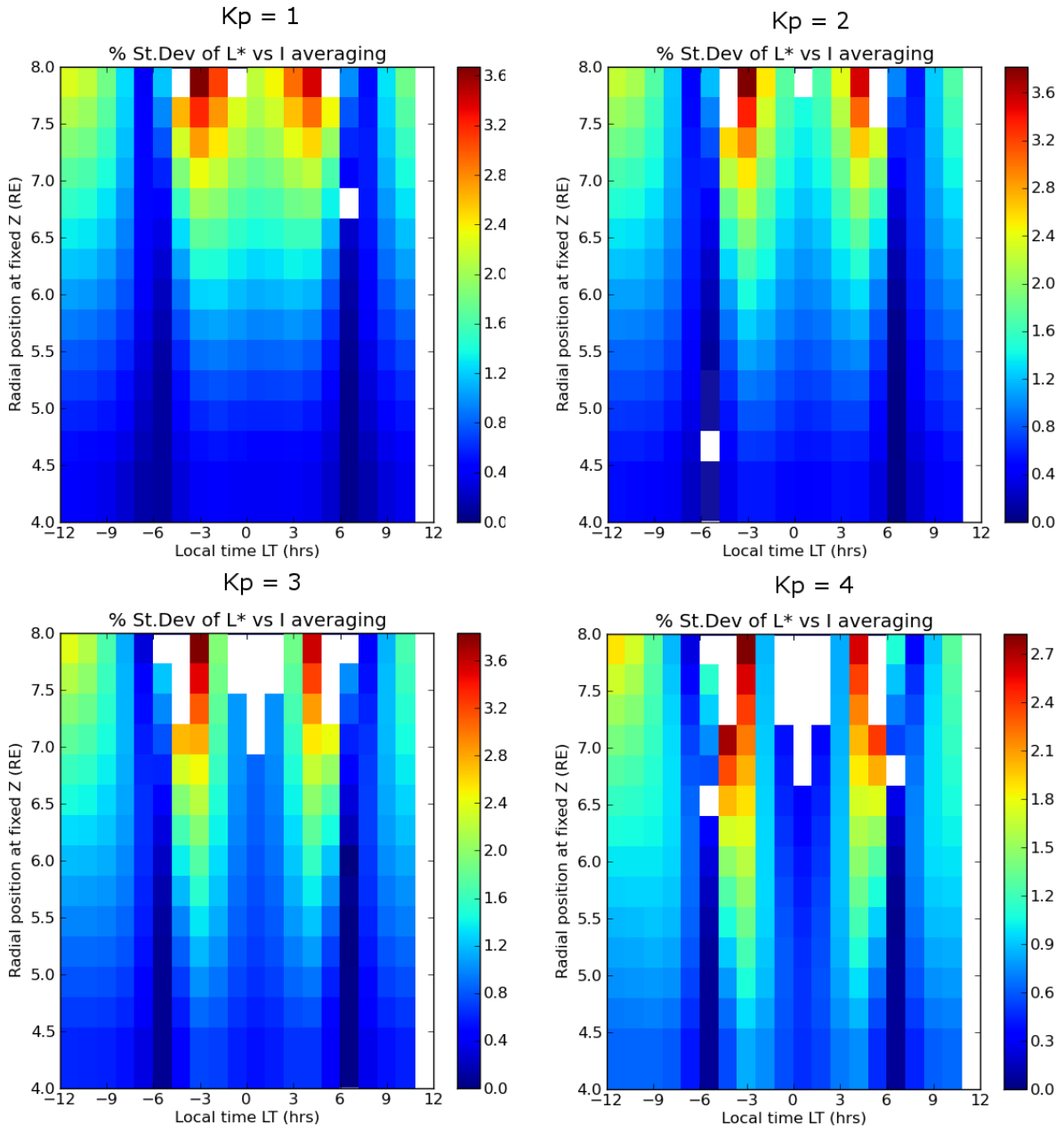

Figure 2: Figure 2. Error in the $\langle L^* \rangle$ approximation, calculated as $Var(L^*)/\langle L^* \rangle$ for each spatial bin, and for a range of Kp values. White pixels indicate where the L^* calculation did not converge. Please note the slight differences in the colorbar magnitudes.

As Kp increases and the geomagnetic field contracts, potentially dragging the drift shells along with it, we see

the error associated with the $\langle L^* \rangle$ approximation propagate Earthward as well. However the magnitude in the error does not increase significantly, rather the relative error associated with particular drift shells change. This implies that when Kp increases, the difference in L^* for neighboring drift shells can become large, making this approximation valid only out to lower L-shells. Again considering Fig.1, it is evident that at a given I a quadratic fit for $L^*(Kp)$ may be sufficient. Averaging over the I dependence described above, the low order approximation becomes

$$\langle L^* \rangle \approx b_2(Kp)Kp^2 + b_1(Kp)Kp + b_0(Kp) \tag{7}$$

where the coefficients $b_2(Kp), b_1(Kp), b_0(Kp)$ may be obtained with numerical fits.

In Figure 3, plots similar to those in Fig.1 are shown, but at $Z_{GSM} = 1R_E$, $R = 6.7R_E$. These plots illustrate drift shells that map further into the tail compared to the plots in Fig.1, but the weak dependence of L^* on I is once again apparent. Thus we may consider Equation 7 as a reasonable approximation even for field lines or drift shells that map to the near-tail, although the associated errors do increase, especially near midnight where the field topology is almost purely determined by external mechanisms.

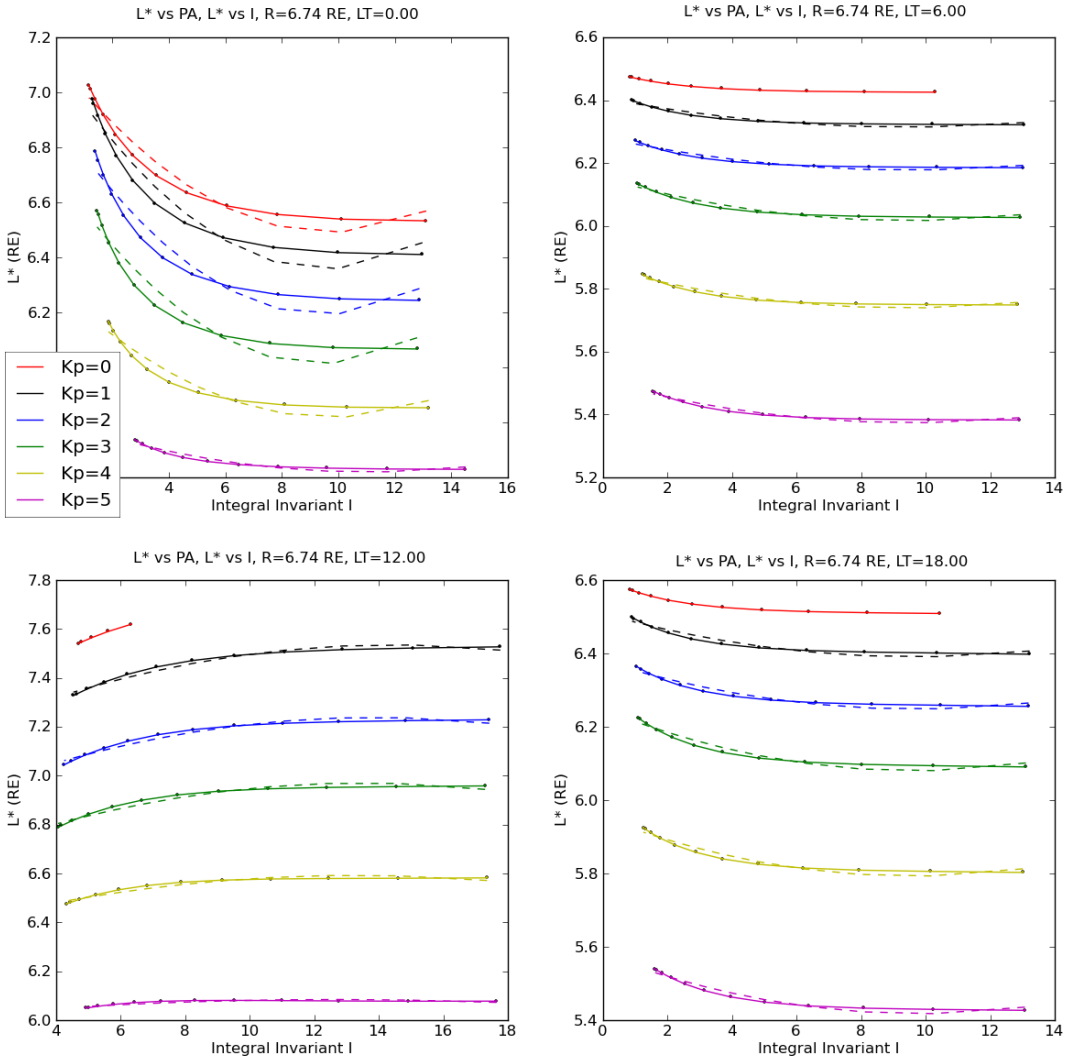

Figure 3: Figure 3. $L^*(I, Kp)$ is shown for a range of α, Kp, at 4 cardinal locations at $6.7R_E$, with $Z_{GSM} = 1R_E$. The dependence of L^* on Kp dominates over the I dependence, suggesting a low order approximation to the I dependence as in Fig.1.

4. Future Direction

The next stage of this research is to convert the L^* dependence on $\vec{x}, t$ into a dependence on ψ, ϕ. This will allow for a more physical interpretation without necessarily knowing the drift shell topologies. Once this dependence is determined, fits to the coefficients in Equation 7 may be calculated, and a more thorough error analysis associated with the $\langle L^* \rangle$ approximation may be undertaken. Separable fits of the form

$$L^*(I, Kp) = L_1^*(I) L_2^*(Kp) \tag{8}$$

or quasi-separable fits of the form

$$L^*(I, Kp) = L_1^*(I) L_2^*(Kp) + \epsilon(I, Kp) \tag{9}$$

where $\epsilon / L^* << 1$ may also be sought to improve correlation between the analytic model and the L^* values calculated from drift shell tracing.

An alternative approach is to consider L^* as a perturbation to the McIlwain L, still in the parameter space defined by I, Kp, ψ, ϕ. Results from a linear perturbation theory would probably not be adequate, but a quasi-linear approach may produce acceptable results. This perturbative approach is still in the planning phase, but the work presented in this report will help determine the sensitivity that L^* exhibits to perturbations in particular parameters, specifically I, Kp. Since calculating L is computationally inexpensive, and since radiation belt studies will cover a fairly limited region of L-shells, this approach may prove to be more tractable.

References

Green, J.C., Kivelson, M.G., 2004. Relativistic electrons in the outer radiation belt: Differentiating between acceleration mechanisms. Journal of Geophysical Research 109.

Roederer, J.G., 1970. Dynamics of Geomagnetically Trapped Radiation. Springer Verlag.

Schulz, M., Lanzerotti, L., 1974. Particle Diffusion in the Radiation Belts. Springer-Verlag, New York.

Tsyganenko, N.A., 1989. A magnetospheric magnetic field model with a warped tail current sheet. Planet. Space Sci. 37, 5–20.

Solar Energetic Particles Trapping in the Magnetosphere

Miles A. Engel

Dartmouth College

Brian A. Larsen

Los Alamos National Laboratory

Abstract

Solar energetic particles (SEPs) are protons, electrons, and heavy ions emitted from the Sun with energies spanning tens of keV to GeV. They are episodic and associated with energetic events at the Sun such as coronal mass ejections (CMEs). Importantly, they can be injected into and trapped by the Earth's magnetosphere, forming transient new, intense radiation belts that can severely damage components of our space infrastructure and cause significant backgrounds in instruments on national security and other payloads. Our goal is to understand the conditions under which SEPs become trapped and untrapped in the magnetosphere, how trapping depends on the energy distribution of the trapped particles, and if we can predict the location and persistence of these new radiation belts. Previous studies have shown how trapping can occur for individual shock-driven events but do not explore the overall magnetospheric conditions that can lead to SEP trapping and cannot predict trapped population energy spectra, location, or provide a probabilistic model trapping likelihood. Using SPEs spanning 10 years, we categorize the events into trapping, untrapping, and no change events. From the characterization similarities are addressed to look for commonalities among members of the groups. The ultimate goal is to answer, what is the probability of trapping injected SEPs based on different magnetospheric conditions, and can we use this probability as a predictive tool?

Citation: Engel, M. A. and B. A. Larsen (2011), Solar Energetic Particles Trapping in the Magnetosphere, Los Alamos Space Weather Summer School Reports 2011, pp. 19–25, LA-UR 12-00074, ISBN 978-0-9850208-1-1

1. Background

1.1. What is a Solar Proton Event?

The National Oceanic and Atmospheric Administration (NOAA) classifies a Solar Proton Event as having occurred whenever three consecutive data points from the Geostationary Operational Environmental Satellites (GOES) are above ten particle flux units (pfu) .[1] (Shea and Smart (1990)) The event is said to end whenever the data points drop below ten pfu. These events are heavily tied to the solar cycle with the vast majority of them occurring during solar maxima. To give an idea of the relative frequencies, fifty four events were recorded during the last solar maxima from 2000-2002, but only twenty were recorded from 1993-1999. The lengths of the events are also heavily modular with some lasting as long as three days and others lasting only an hour or two.

1.2. What is trapping?

Trapping is the process of energetic particles being injected into the Earth's magnetosphere and forming new radiation belts consisting of the injected particles. Not all events cause trapping and the current mechanism for the actual trapping to occur is unknown. It is believed that a shock wave must be associated with the incident particles (Selesnick et al. (2010); Kress et al. (2004)) so that they can be injected deep enough into the magnetosphere to become trapped, but shocks have been observed with no associated trapping and so that it may be a necessary condition but it is not sufficient.

[1] 1 pfu = 1 p cm^{-2} sr^{-1} s^{-1}

1.3. Polar Operational Environmental Satellites (POES)

POES are a set of polar orbiting satellites, operated by NOAA, with several different instruments used for a variety of Earth and Space based observations. Included on all satellites is the Space Environment Monitor package that has a suite of detectors designed to measure electron and proton count rates at a variety of energies(Evans and Greer (2004)). For this study we used the four omni-directional integral proton detectors, with energy cutoffs of >16MeV, >36MeV, >70MeV, and >140MeV. The satellites themselves are in different phased sun-synchronous orbits with average altitudes of 850 km and periods of about 102 minutes.

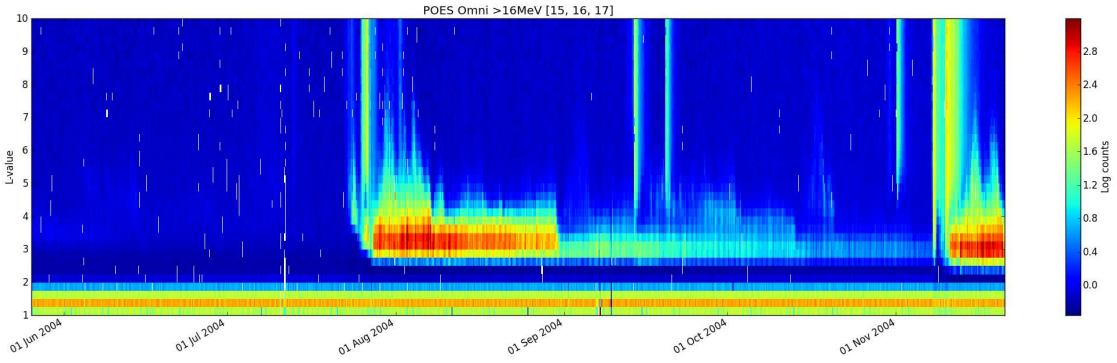

Figure 1: A 6 month excerpt from the >16MeV omnidirectional POES data set from satellites -15, -16, -17. It is time averaged at 300 minutes, and L averaged in 0.25 bins. The dates are from 05-26-2004 to 11-21-2004 (180 days). There are five clear SEP events during this time.

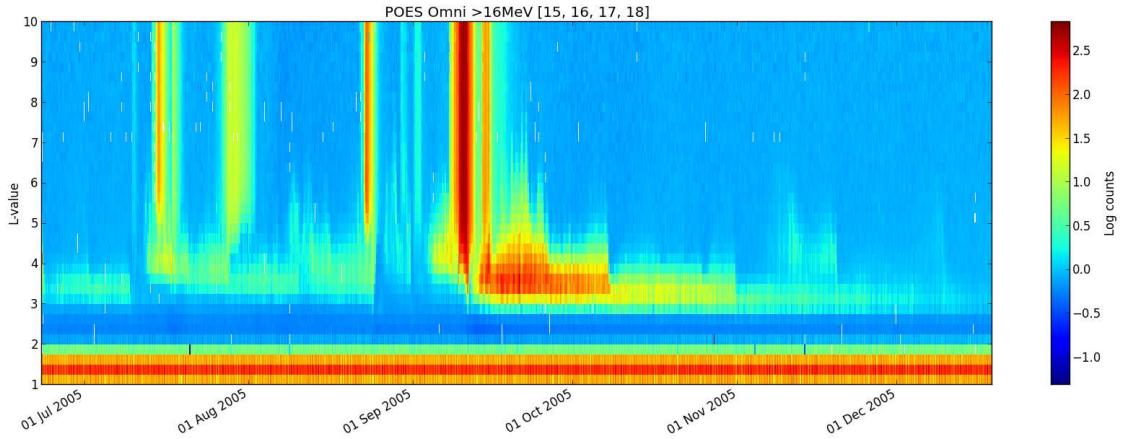

Figure 2: A 6 month excerpt from the >16MeV omnidirectional POES data set from satellites -15, -16, -17. It is time averaged at 300 minutes, and L averaged in 0.25 bins. The dates are from 06-23-2005 to 12-19-2005 (180 days). There are four events recorded during this time, with the possibility of two or three other events that did not reach 10 pfu at GOES.

2. Characterization of Events

2.1. Data set

Using the last eleven years of data to have a representative subset of the full data. [2] The chosen data set from POES-15, -16, -17, -18, and -19 contains 85 SEP events (as classified by NOAA)[3], thirteen of which have data for

[2]Data is available for POES starting from 1979 to present with varying numbers of spacecraft.
[3]http://umbra.gsfc.nasa.gov/SEP/

one satellite available, thirty three have two satellites, twenty five have three satellites, seven have four satellites, and seven have five satellites. These detectors do not yet have fully derived flux conversion factors forcing us to use counts for this study. The instruments are very similar so it is assumed that the counts can be combined with equal weighting. This assumption will be revisited in the future but will not affect the results of this work.

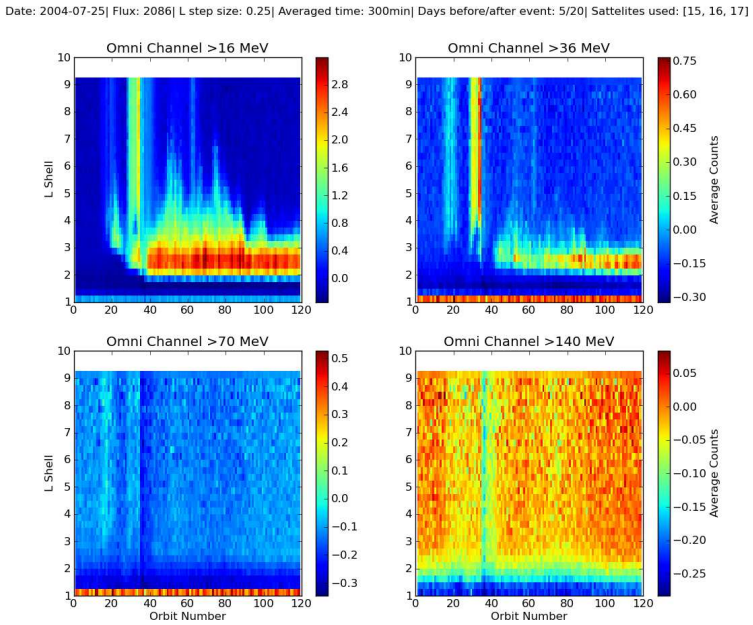

Figure 3: Characteristic Trapping Event: This is a close up view of a trapping event as observed in all four omni-directional energy channels. The binning is the same as in figures 1 and 2 with 300 minute time averages and 0.25 L value averages. This event took place on 7-25-2004

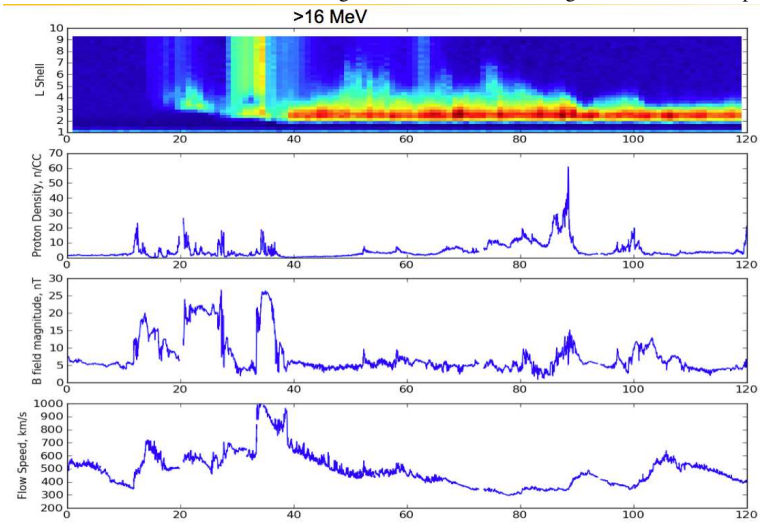

Figure 4: Characteristic Trapping Event: View of the >16 MeV omnidirectional POES data set along with several of the ACE SWEPAM solar wind parameters. (Proton density, B field magnitude, and flow speed).

2.2. Analysis

In order to properly analyze the events it was first necessary to characterize each event and to determine if there was any trapping or untrapping that occurred. To do this images were generated for the entire time range (Figure 1

and 2) and each event identified as either a trapping, untrapping , or no change event. A trapping event was said to have occurred if there was a noticeable increase in particle count rates in the range of L=2 to L=4 after the event was finished, where as an untrapping event was said to have occurred if there was a marked drop off of particle counts in the same L values. As can be seen from figures 1 and 2 it was usually relatively simple to identify an event as either trapping or untrapping but could become much more challenging when events occurred in close proximity to each other, or were overshadowed by stronger events that caused trapping prior to the event. It is also worth noting that it was possible for an event to have little to no impact on the particle count rates, these events were labeled as no-change events. Final determination of an events classification was made by generating event specific figures to better determine the type.

2.2.1. Characteristic trapping event

In figure 3 there is a substantial increase in particle counts in the first two energy channels beginning at orbit 40, indicating that this is a trapping event. Figure 4 shows the>16 MeV channel along with three of the solar wind parameters during this time, with a large increase in all three being the indication of a shock. Note that these shocks are not coupled to the events themselves since the travel times for highly energetic particles is much smaller than that of the shocks travel time. This shows that a shock occurs during the event, which is in agreement with previous work done. (Kress et al. (2004)). Figure 4 overlays the ACE-SWEPAM (McComas et al. (1998)) solar wind data demonstrating the shock arrival coincident with the SEP enabling the trapping. These coincidences seem to be required for trapping to occur.

2.2.2. Characteristic untrapping event

In figure 5 there is a sudden drop off of particle counts in the first energy channel signifying this as an untrapping event. The solar wind parameters (figure 6) show that there is a large shock which occurs after the event that coincides with the drop off of counts. Whether the event itself was necessary or if the untrapping occurred solely because of the shock needs further investigation.

2.2.3. Characteristic no change event

In figure 7 there is very little change in particle counts from before to after the event in any of the four energy channels. Figure 8 shows that there is no associated shock occurring during the event. Interestingly we see a large shock occurring long after the event but corresponding to an untrapping of particles. This seems to imply that an event isn't necessary for untrapping to occur and that the properties of the solar wind are more important.Figures 3-7 show a characteristic event for each type so that it is more clear how these determinations were made.

2.2.4. Unexplained event

While figures 3-8 show relative consistency with each other, there are still many examples that are not as easily classified. Figure 9 shows a strong shock occurring during an event much like in figure 4, but with no associated trapping occurring. Implying that while a shock may be a necessary condition for trapping to occur, it is not sufficient and there must be other conditions needed for trapping to occur.

2.3. Results

Of the 85 events analyzed 14 (17%) were classified as trapping events, 18 (21%) were classified as untrapping events, and 53 (62%) were classified as no-change events. This means that on average an event is more likely to not cause any change then it is to cause either trapping or untrapping. Figures 3-7 show a characteristic event for each type so that it is more clear how these determinations were made. In addition the solar wind parameters allow these events to be further characterized depending on the presence and location of a shock. For the trapping events there was always an associated shock which occurred during the event itself. The untrapping events were also associated with a shock, but the event itself wasn't necessary and often untrapping would occur without any event present. The no-change events are the hardest to classify as a shock may occur during these events and cause no noticeable change in the particle counts.

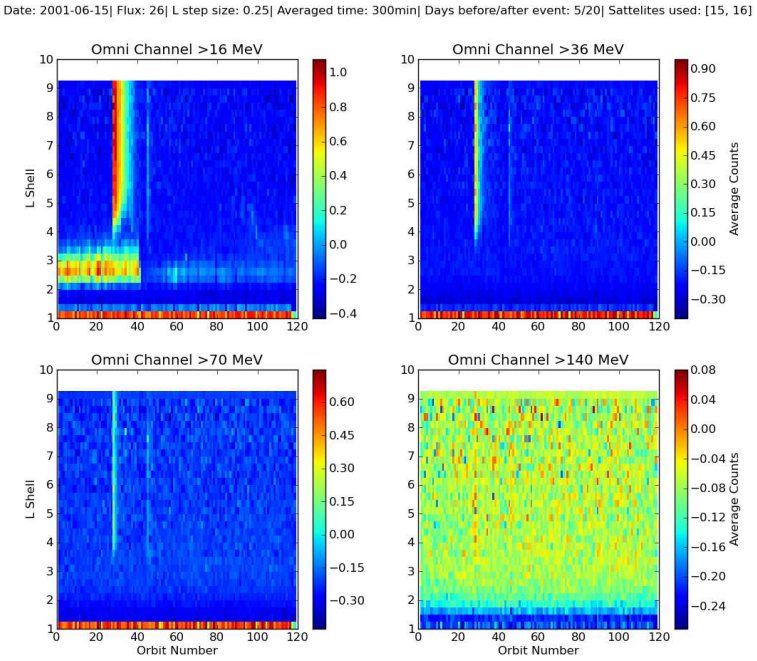

Figure 5: Characteristic Untrapping Event: This is a close up view of an untrapping event as observed in all four omni-directional energy channels. The binning is the same as in figures 1 and 2 with 300 minute time averages and 0.25 L value averages. This event took place on 6-15-2001. Note that there is still a small belt after the event, but it is drastically decreased.

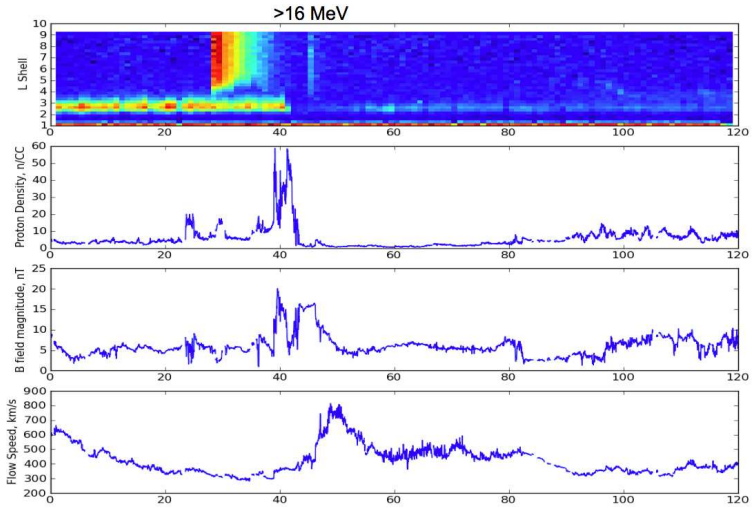

Figure 6: Characteristic Untrapping Event: View of the >16 MeV omnidirectional POES data set along with several of the solar wind parameters. (Proton density, B field magnitude, and flow speed).

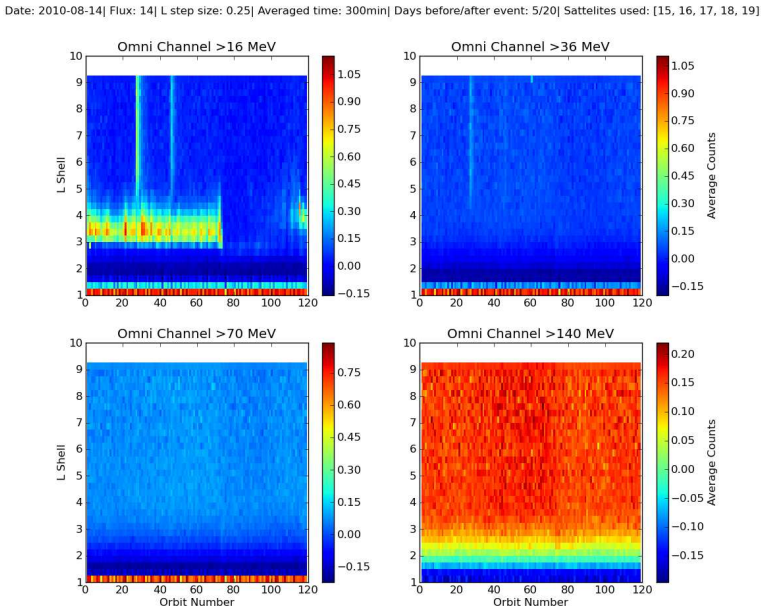

Figure 7: Characteristic No-Change Event: This is a close up view of a no-change event as observed in all four omni-directional energy channels. The binning is the same as in figures 1 and 2 with 300 minute time averages and 0.25 L value averages. This event took place on 8-14-2010. Note that there is a sharp drop off long after the event took place, but there is virtually no change during the event itself.

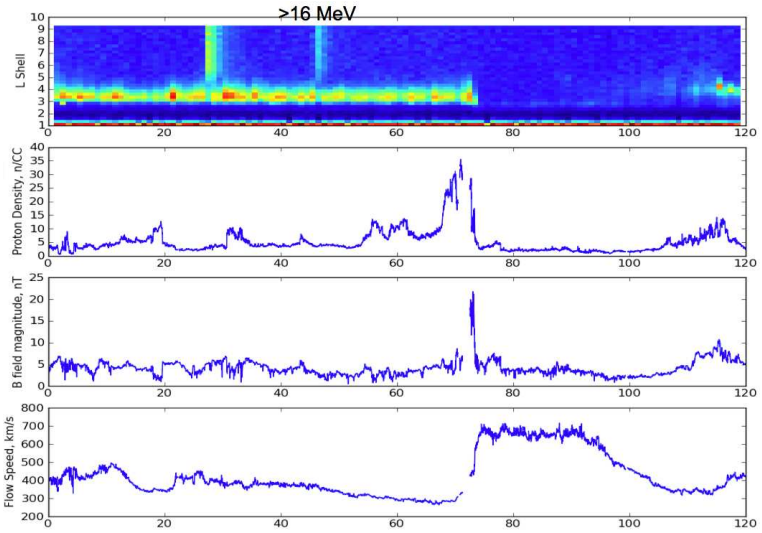

Figure 8: Characteristic No-Change Event: View of the>16 MeV omnidirectional POES data set along with several of the solar wind parameters. (Proton density, B field magnitude, and flow speed).

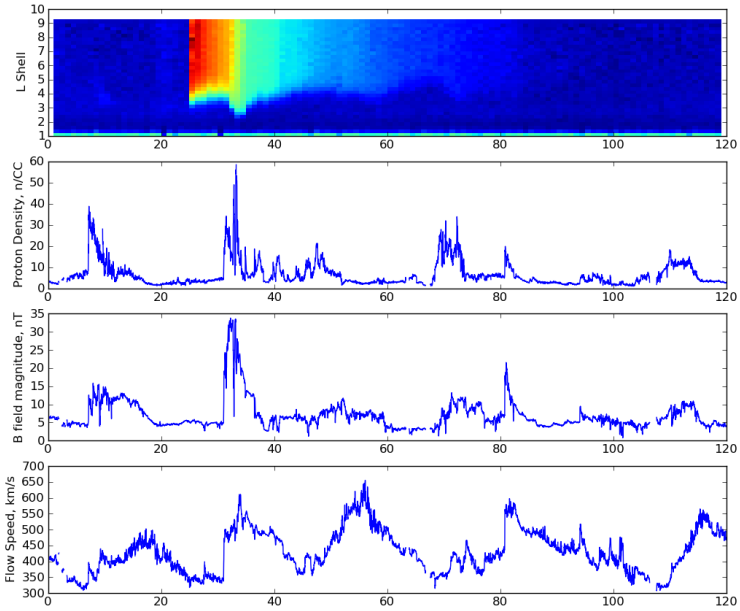

Figure 9: Unexplained Event: View of the >16 MeV omnidirectional POES data set along with several of the ACE-SWEPAM solar wind parameters. (Proton density, B field magnitude, and flow speed).

3. Conclusion

SEP events are complicated processes with many variables effecting the outcome of the event. This study begins to take apart each of these events in the hopes of being able to understand the methods by which particles can become trapping and untrapped in the magnetosphere. While shocks seem to play a crucial role in the trapping and untrapping of particles they are not sufficient in determining the outcome of these particles. Now that the SEP events are characterized studies can begin on the similarities and differences among and between events in the different categories.

References

Evans, D.S., Greer, M.S., 2004. Polar Orbiting Environmental Satellite Space Environment Monitor–2 Instrument Descriptions and Archive Data Documentation. Technical Report. NOAA Tech. Mem. 1.4, Space Environ. Lab., Boulder, Colorado.

Kress, B.T., Hudson, M.K., Perry, K.L., Slocum, P.L., 2004. Dynamic modeling of geomagnetic cutoff for the 23–24 november 2001 solar energetic particle event. Geophys. Res. Lett. 31.

McComas, D., Bame, S., Barker, P., Feldman, W., Phillips, J., Riley, P., Griffee, J., 1998. Solar wind electron proton alpha monitor (swepam) for the advanced composition explorer. Space Science Reviews 86, 563–612. 10.1023/A:1005040232597.

Selesnick, R.S., Hudson, M.K., Kress, B.T., 2010. Injection and loss of inner radiation belt protons during solar proton events and magnetic storms. J. Geophys. Res. 115.

Shea, M.A., Smart, D.F., 1990. A summary of major solar proton events. Solar Physics 127, 297–320. 10.1007/BF00152170.

Do substorm injections cause EMIC waves?

S. H. Lee

Geophysical Institute, University of Alaska, Fairbanks, Alaska, USA.

S. K. Morley

Los Alamos National Laboratory, Los Alamos, New Mexico, USA.

Abstract

Substorms are known to drive a temperature anisotropy in hot ions, which is a source of free energy for Electro-Magnetic Ion Cyclotron (EMIC) waves. EMIC waves have been observed at and after substorm onset by case studies, but no clear evidence of substorms causing EMIC has been shown. We investigate the association of EMIC waves with substorm injections, at least at geosynchronous orbit. An automated search engine has identified 488 substorm events during 2007 and 346 of these substorms have been confirmed by comparison with LANL geosynchronous particle data. High-resolution data from the GOES-11 and 12 geosynchronous satellite magnetometers have been used provide a comprehensive catalog of EMIC wave activity during 2007. For the 1922 EMIC wave events identified, 150 (7.8 %) occurred within one hour after substorm onset. The peak power spectral densities of the EMIC waves are not correlated with the magnitude of the substorm. We assess the statistical association between substorm onset and EMIC waves to determine whether substorm injections significantly affect EMIC wave generation. We present the results of this study and discuss some further work required to unambiguously answer this question.

Citation: Lee, S. H. and S. K. Morley (2011), Do substorm injections cause EMIC waves?, Los Alamos Space Weather Summer School Reports 2011, pp. 26–33, LA-UR 12-00074, ISBN 978-0-9850208-1-1

Keywords: Substorm, EMIC waves, Association Analysis

1. Introduction

The inner magnetosphere is a region whose dynamics are strongly affected by the ring current. The interaction of waves generated in the inner magnetosphere with the Van Allen radiation belts can lead to relativistic electron precipitation (REP) which penetrates into the middle and lower stratosphere and can change global ozone levels (Callis et al., 1991). Turunen et al. (2009) described how the particle precipitation creates odd nitrogen and odd hydrogen in the upper atmosphere, which can affect ozone chemistry.

Several possible mechanisms have been proposed to account for the REP from the radiation belts. One of these mechanisms is wave-particle interactions. Circularly polarized wave modes through cyclotron resonance, for example, whistler-mode chorus and electromagnetic ion cyclotron (EMIC) waves can be generated, and by resonance with electrons gyrating in a magnetic field can cause pitch angle scattering and hence electron precipitation (Lorentzen et al., 2000). In other words, EMIC waves, which are the focus of this paper, resonate with the relativistic electrons (MeV) from the radiation belts and can drive loss through precipitation into the atmosphere (Summers, 2005). EMIC waves occur in the Pc1-Pc2 frequency range (0.1-5 Hz) and can often be observed in three distinct bands, below the gyrofrequencies of H^+, He^+, and O^+. EMIC waves are known to grow near the magnetic equator along the high-density duskside plasmapause, which is a preferred region for proton cyclotron instability, as left-handed waves (Fraser and Nguyen, 2001). Wave growth is driven by anisotropic ring current (1-100 keV) protons, which are injected into the inner magnetosphere by enhanced earthward convection during geomagnetic storms and substorms. Therefore many studies about the relationship between EMIC waves and geomagnetic storms and substorms have been carried out.

Email addresses: slee111@alaska.edu (S. H. Lee), smorley@lanl.gov (S. K. Morley)

Ground-based observations of Pc1 pulsations, which are typically electromagnetic ion cyclotron waves, occur ≈4-5 times more frequently several days after the minimum Dst of isolated, intense geomagnetic storms (Bortnik et al., 2008). Another statistical analysis of wave occurrence has been indicated that EMIC waves at low L occurred 5 times more often at storm times than during quiet times (Erlandson and Ukhorskiy, 2001). More recently, Halford et al. (2010) found that 1.6 times more EMIC waves occured during storm than nonstorm times over the CRRES mission. Simulation of the growth rate of EMIC waves between the oxygen and helium gyrofrequencies, as the storm evolves, has shown agreement with the observation that EMIC waves occur primarily during the main phases of storms (Jordanova et al., 2001). Superposed epoch analysis of 22 storms has shown that 78% of wave events in the He-band occur during the main phase; conversely, H-band emissions were found to be preferentially excited during the recovery phase (Fraser et al., 2010). Thus, many theoretical and observational studies of EMIC waves and their relationship with different definitions of a geomagnetic storm and with various storm phases have suggested different conclusions.

Several plasma waves are associated with particle injections into the magnetosphere during substorm onset. The newly-injected energetic ions drift westward through the evening sector and can enhance existing, or generate new, EMIC waves along their trajectory as long as the temperature anisotropy is maintained. One type of EMIC waves is Intervals of Pulsations of Diminishing Periods (IPDP). IPDP are characterized by an increasing frequency from 0.1 to 1-2 Hz, and can be generated through the ion cyclotron resonance mechanism where energy is exchanged to the waves from the westward drifting hot particles injected into the magnetosphere during the substorm. The IPDP events may occur with a time delay with respect to the substorm activity in the midnight sector (Pikkarainen et al., 1983; Mursula et al., 2000). EMIC waves, including IPDP, have been observed at and after substorm onset and several case studies have been presented, but no clear evidence of substorms causing EMIC waves has been shown. Therefore it is important to study the statistical association of EMIC waves (and the conditions under which they occur) with substorms. In this paper we investigate the association of EMIC waves with substorm injections at geosynchronous orbit through 2007.

2. Data sets

2.1. Electromagnetic Ion Cyclotron waves Identification

EMIC waves are generated near the magnetic equator along the high-density duskside plasmapause, which is a preferred region for the proton cyclotron instability, and occur in the Pc1-Pc2 frequency range (0.1-5Hz) as left-handed waves. High resolution data from the GOES-11 and 12 geosynchronous satellites provide a comprehensive catalog of EMIC wave activities during 2007. The data were provided by B. J. Fraser (personal communication, 2010). For the 1922 EMIC wave events identified, the occurrence peaked in the afternoon sector, at about 16 LT; this result is not shown in this paper, but is in agreement with previous results. Of these events, 150 (7.8 %) occurred within one hour after identified substorm onsets.

2.2. Substorm Identification

In this paper we use a list of 488 substorm onsets in 2007 that were determined using a mechanistic method of substorm identification, the search engine SSeeker, first described by Tanskanen (2009). The list of onsets was generated and supplied by E. Tanskanen (personal communication, 2011). The substorm onsets are identified using the IL index, by inspecting the data for a rapid and prolonged drop in the index. The IL index is created by computing an envelope of the north–south magnetic field component of the IMAGE magnetometer network measurements in Fennoscandia. Thus the IL index is a local time analog of the AL index. The IMAGE network gives excellent latitudinal coverage and enables capturing of the substorms during all geomagnetic activity levels (Tanskanen, 2009). The optimal IMAGE ground-based network coverage is about 16:00-03:00 UT. 488 substorm onsets were identified by the SSeeker search engine, however ground magnetic bays are not universally accepted as an unambiguous signature of substorm activity; particle injections at geosynchronous orbit are a robust feature of substorms. Since we are interested in the energetic particle injections, we visually inspected the available SOPA energetic particle data, from LANL spacecraft, and found 346 out of 488 substorms to have an associated particle injection.

3. Results

In order to answer the main question for this paper, we first examined the conditions of geomagnetic activity under which EMIC wave activity occurs, measured by Kp index. Figure 1 (top panel) shows the distribution of occurrence probability of Kp as a function of Kp index: for all measured Kp (green line); Kp during observed EMIC waves (blue line); and Kp during EMIC waves within 1 hour after the substorm onset (red line). The probability distribution is skewed to higher values at times of EMIC observation, as might be expected from the requirement of anisotropic ring current ions. For those EMIC events occurring in close coincidence with substorm onsets, the distribution is also skewed to higher values, and occurrence probabilities are extremely low below Kp≃1+. By contrast, the most likely value of Kp (considering all times) is less than 1. The bottom panel of Figure 1 shows the cumulative distribution functions for each case presented in the top panel. The fiftieth percentiles for each case increase from all times (∼ 1), through EMIC observation times (∼ 2+), to cases of coincident EMIC and substorm onset (∼ 3).

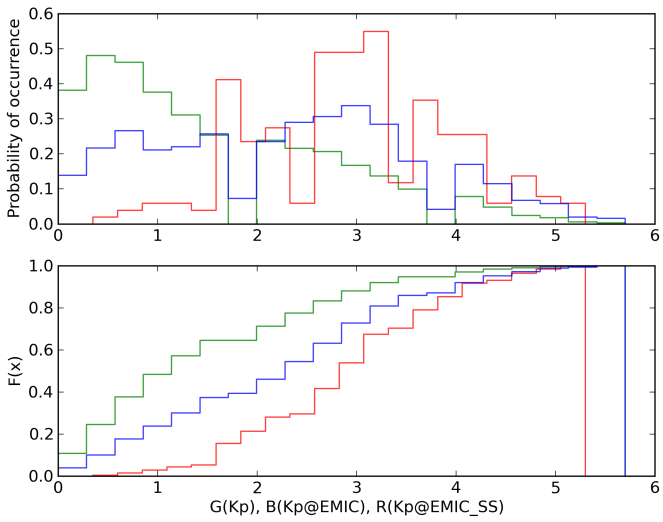

Figure 1: The probability distribution (top) and the cumulative probability distribution (bottom) of Kp, for three cases: all Kp (green line); Kp during EMIC (blue line); and Kp during EMIC within 60 minutes of substorm onset (redline). EMIC waves occur under higher Kp than average.

We also investigated the relationship between the substorm bay magnitude and the strength of the EMIC observed, as measured by the peak wave power. For each EMIC wave event which occurs within 1 hour after substorm onset (number of events = 150) we found the minimum value of IL during the substorm. Figure 2 shows the peak (substorm-associated) EMIC wave power as a function of magnitude of substorms, as measured by the magnetic bay magnitude. There is no clear relationship between these variables, indicating that the size of the substorm (using bay magnitude as a proxy) is unrelated to the magnitude of the observed EMIC waves.

To illustrate the analysis employed later in the paper, we briefly present a single event from the database. Figure 3 shows one substorm event which is associated with EMIC wave events. The top two panels show the IL index for a substorm interval identified by the SSeeker algorithm (top panel), the hot ion temperature anisotropy (second panel) $T_{\perp}/T_{\parallel}$. The interval is from from 19:00–22:00 UT. The red dashed line indicates substorm onset at 19:17 UT, which is the starting point of the substorm expansion phase, and the three blue dashed lines are the onsets of EMIC wave activity observed at GOES-12. The lower panel shows the SOPA proton data from two LANL spacecraft data over the interval 18–24 UT on March 5th 2007. This substorm event is confirmed by comparison with LANL geosynchronous particle data. The particle injection is indicated by the white arrow marked at 19:16 UT. The reason we plot the anisotropy is that this condition can drive wave growth; the data shown here confirm that the EMIC wave activity arises under the anisotropy condition $T_{\perp}/T_{\parallel} > 0$ for this case.

Figure 4 shows a schematic of the relative locations of the observing platforms, both ground- and space-based. The yellow shaded regions represent the area covered by the IMAGE magnetometer array at either end of the UT interval

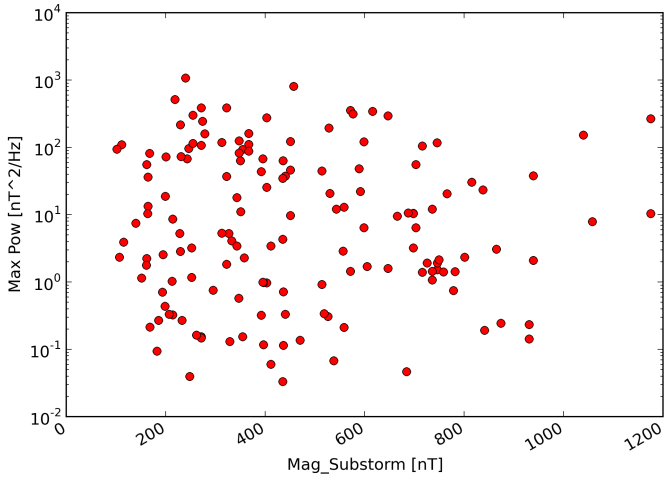

Figure 2: iScatter plot of maximum power of EMIC waves against substorm magnitude for 2007.

used for substorm identification with SSeeker. The configuration for the presented case study is also displayed on this figure. It shows the local times of the spacecraft, marked by filled symbols, and the coverage of the IMAGE magnetometers at 18–24 UT on 5 March 2007. The region bounded by black lines around 19±1.5 LT is the approximate area covered by the IMAGE array and includes the longitude of the LANL-01A spacecraft used to detect the particle injections presented. Thus the timing of particle injections and the ground-based substorm onset is approximately the same. GOES-12 detected EMIC wave activity about ~10 minutes and ~20 minutes after the substorm onset, which is also in reasonable agreement with the expected drift time for protons. Following the result of Lorentzen et al. (2000), 60 keV protons are expected to take around 24 minutes to drift from LANL-01A to the observation location of GOES-12. The ideal configuration would be in the day when a geosynchronous LANL satellite is closer to midnight and the GOES satellites are closer to dusk, with magnetometer coverage in the midnight and dusk sectors.

We assess the statistical association between substorm onset and EMIC waves to determine whether substorm injections significantly affect EMIC wave generation. We do this using association analysis, described by Morley and Freeman (2007), and implemented in the software package SpacePy (Morley et al., 2011). Association analysis tests how many events are coincident between two series of discrete events. Here we call series A the occurences of EMIC waves during 2007 and series B is the set of substorm onsets in 2007 identified by SSeeker and confirmed by visual inspection of the LANL particle data.

The association number, n(u, h), is the number of EMIC waves within a half window ±h of the substorm onset as a function of time lag (u) which is calculated as $n(u,h) = \sum_{i=1}^{N} \#\{\left|b_j + u - a_i\right| < h\}$ where $\#X$ denotes the number of elements in the set X and $a_i (i \in \{1, 2, \ldots N\})$ and $b_j + u (j \in 1, 2, \ldots M\})$ are the times for the two points from each event, respectively. We want to test the null hypothesis that there is no association between two events A and B for any lag u. The alternative hypothesis is therefore that there is an association. To assess the association expected by chance we look at the asymptotic association number, that is the value that the association number tends to as the time lag (u) tends to infinity. This gives the association expected by chance because we can expect independence between the two series to be imposed by a sufficient separation in time to break any physical correlation. Thus, in the case that there is no significant deviation of the association number from its asymptotic value at any lag, the null hypothesis is accepted. In the case that the alternative hypothesis is correct, we expect to see a significant peak from the asymptotic level at some lag.

Figure 5 (a) shows the calculated association number as a function of lag. There is a clear peak above the asymptotic association number which is marked by the red dashed line in the middle of the plot. This suggests that substorm onsets are associated with the onset of EMIC waves. However, a closer look reveals that the timescale chosen for

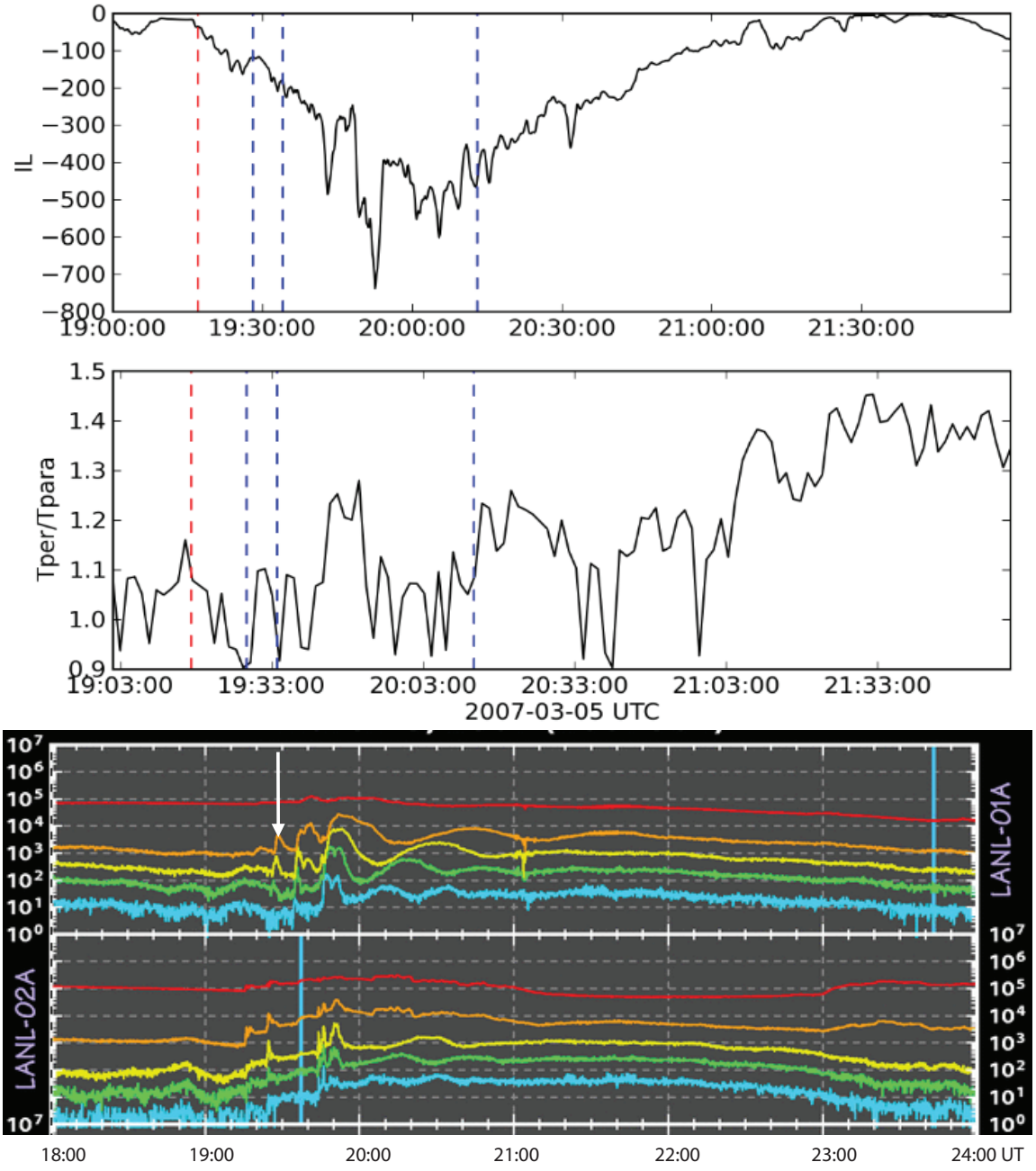

Figure 3: A substorm event on 5 March 2007 at 19:00–20:00 UT. The three panels show: (top) the IL index; (middle) the temperature anisotropy ($T_\perp/T_\parallel$); (bottom) energetic particle data from the SOPA instruments on LANL-01A and LANL-02A. The red dashed line indicates substorm onset at 19:17 UT, the blue dashed line marks EMIC waves observed by GOES-11 and 12 at 19:28, 19:34, 20:13. The white arrow marks the onset of particle injections at 19:16 UT at LANL-01A.

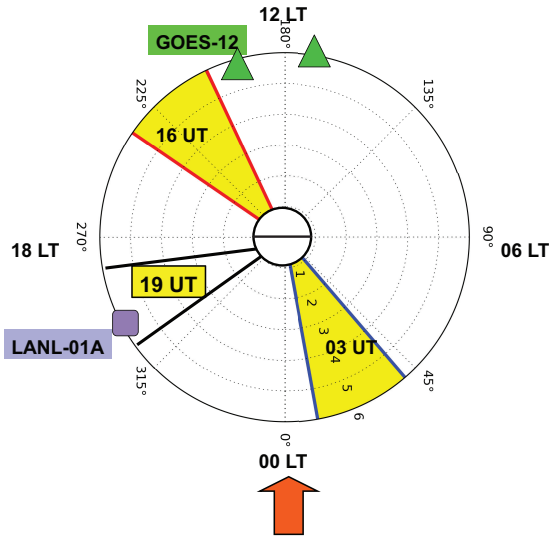

Figure 4: A schematic presentation of the relative locations of the instruments used in this paper. The specific configuration for the case study (figure 2) is also shown. It shows the location of the satellites and the optimal IMAGE ground-based network coverage which is 16-03 UT (11 hours). The two triangles represent GOES-12 and 11 and the square marks the location of LANL-01A for the presented case study. The yellow cones show the coverage of the IMAGE magnetometer array for each marked time period (the bounds of the interval used for substorm identification by SSeeker). The black lines mark the area covered by the IMAGE array during the example event. The red arrow marks local midnight.

plotting this parameter is insufficient. While any causative time-scales should be vastly exceeded by the largest lags examined (4 hrs), expanding the range of lags further shows evidence of an aliasing effect due to the observational setup; the result of expanding the range of lags from which is shown in Figure 5(b). At large separation n does not tend to a mean asymptotic association number, instead a periodicity of approximately 1 day can be seen. This has been determined to arise from the fixed relative locations of the ground- and space-based observations used. The substorm cycle occurs continuously, and is unrelated to the universal time of observation. The fixed local time sector of the IMAGE array will maximize the occurrence of substorm onset as the array passes through the pre-midnight sector. Similarly, the probability of observing EMIC waves will maximize as the GOES satellites pass through the late afternoon/dusk sector. Thus the combination of the relative locations of the GOES satellites and the IMAGE array will lead to a diurnal variation in the association number. However, we expect that at separations of $|u| \geq 24$ hours the phasing between events in each series will be randomized and thus a significant association could be identified by a difference in the peak heights due to phase randomization.

4. Discussion and Conclusions

This study of the relationship of EMIC wave occurrence and substorms is based on GOES satellite results at geosynchronous orbit and IMAGE magnetometer data during 2007. EMIC waves are observed most commonly and most intensely during geomagnetic storms, and particle injections into the magnetosphere during an auroral substorm are associated with several plasma wave events. For instance, IPDP pulsations which are believed to be generated via the ion cyclotron resonance mechanism have been observed at and after the substorm onsets on the ground by case studies. However, there is no statistical evidence to show that substorms directly cause EMIC waves.

In this paper we have studied the statistical association of EMIC waves, and the conditions under which they occur, with substorm onsets. We have found that more EMIC waves occur at higher geomagnetic activity, as measured by Kp, than for average activity conditions throughtout the year. When Kp index is about 3, EMIC waves are observed more often. We also show one case study where the data shows a substorm injection occurring prior to, and possibly causing, observed EMIC waves on 5 March 2007. Due to substorm-related dipolarization, and enhanced convection,

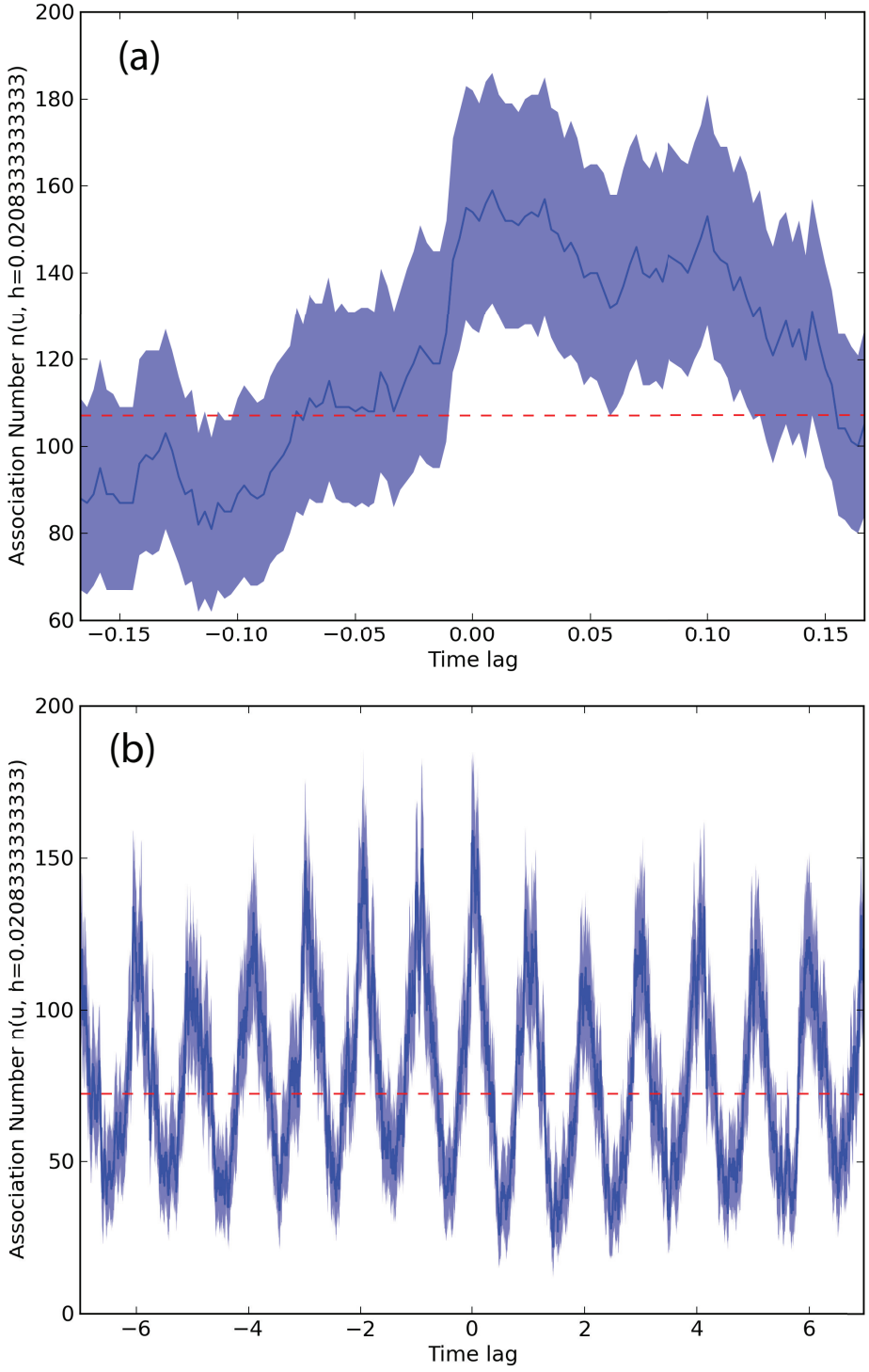

Figure 5: Association number between substorm onset and EMIC wave occurrence within a window of ±h of the onset time as a function of the time lag u in days. The red dashed horizontal line indicates the expected association under independence. (a) The association number is shown when the half window (h) is ±30 minutes and time lag (u) is ± 4 hours (0.17 days). (b) Same as (a) but time lag (u) = ± 7 days.

ions (and electrons) are injected and a westward drift takes place. EMIC waves are then generated by the wave-particle interactions. There is no obvious correlation between the peak power of EMIC waves and the magnitude of substorms (measured by ground magnetic bays).

The results from the statistical study provide limited evidence that the observed substorm onsets and EMIC waves are associated. In particular, less than 10% of the observed EMIC occurred within 1 hour of a detected substorm onset. Further investigation is required to show how much the observing configuration affects the rate of detected coincidences.

Importantly, the association number does not tend to an expected association number with increasing lag. The results obtained here are made more difficult to interpret as peaks in the association are seen with a daily repetition frequency which indicates that the peak in association arises from the configuration of instrumentation, which is fixed in longitude. However, the daily maximum of the association number appears to decrease as the time lag increases, thus further work might be able to distinguish whether there is actually a higher than expected association between EMIC waves and substorm onsets. Thus we conclude that substorm onsets might cause EMIC waves, and to unambiguously answer the question – as well as addressing what fraction might be substorm driven – more work needs to be done. In particular we will need to model the effects of the observational configuration on the association number.

References

Bortnik, J., Cutler, J.W., Dunson, C., Bleier, T.E., McPherron, R.L., 2008. Characteristics of low-latitude Pc1 pulsations during geomagnetic storms. Journal of Geophysical Research (Space Physics) 113, A04201.

Callis, L.B., Boughner, R.E., Baker, D.N., Blake, J.B., Lambeth, J.D., 1991. Precipitating relativistic electrons - Their long-term effect on stratospheric odd nitrogen levels. J. Geophys. Res. 96, 2939–2976.

Erlandson, R.E., Ukhorskiy, A.J., 2001. Observations of electromagnetic ion cyclotron waves during geomagnetic storms: Wave occurrence and pitch angle scattering. J. Geophys. Res. 106, 3883–3896.

Fraser, B.J., Grew, R.S., Morley, S.K., Green, J.C., Singer, H.J., Loto'aniu, T.M., Thomsen, M.F., 2010. Storm time observations of electromagnetic ion cyclotron waves at geosynchronous orbit: GOES results. Journal of Geophysical Research (Space Physics) 115, A05208.

Fraser, B.J., Nguyen, T.S., 2001. Is the plasmapause a preferred source region of electromagnetic ion cyclotron waves in the magnetosphere? Journal of Atmospheric and Solar-Terrestrial Physics 63, 1225–1247.

Halford, A.J., Fraser, B.J., Morley, S.K., 2010. EMIC wave activity during geomagnetic storm and nonstorm periods: CRRES results. Journal of Geophysical Research (Space Physics) 115, A12248.

Jordanova, V.K., Farrugia, C.J., Thorne, R.M., Khazanov, G.V., Reeves, G.D., Thomsen, M.F., 2001. Modeling ring current proton precipitation by electromagnetic ion cyclotron waves during the May 14-16, 1997, storm. J. Geophys. Res. 106, 7–22.

Lorentzen, K.R., McCarthy, M.P., Parks, G.K., Foat, J.E., Millan, R.M., Smith, D.M., Lin, R.P., Treilhou, J.P., 2000. Precipitation of relativistic electrons by interaction with electromagnetic ion cyclotron waves. J. Geophys. Res. 105, 5381–5390.

Morley, S.K., Freeman, M.P., 2007. On the association between northward turnings of the interplanetary magnetic field and substorm onsets. Geophys. Res. Lett. 340, L08104.

Morley, S.K., Koller, J., Welling, D.T., Larsen, B.A., Henderson, M.G., Niehof, J.T., 2011. Spacepy - A Python-based library of tools for the space sciences, in: Proceedings of the 9th Python in science conference (SciPy 2010), Austin, TX.

Mursula, K., Prikner, K., Feygin, F.Z., Bräysy, T., Kangas, J., Kerttula, R., Pollari, P., Pikkarainen, T., Pokhotelov, O.A., 2000. Non-stationary Alfvén resonator: new results on Pc1 pearls and IPDP events. Journal of Atmospheric and Solar-Terrestrial Physics 62, 299–309.

Pikkarainen, T., Kangas, J., Kiselev, B., Maltseva, N., Rakhmatulin, R., Solovev, S., 1983. Type IPDP magnetic pulsations and the development of their sources. J. Geophys. Res. 88, 6204–6212.

Summers, D., 2005. Quasi-linear diffusion coefficients for field-aligned electromagnetic waves with applications to the magnetosphere. J. Geophys. Res. 110, A08213.

Tanskanen, E.I., 2009. A comprehensive high-throughput analysis of substorms observed by IMAGE magnetometer network: Years 1993-2003 examined. Journal of Geophysical Research (Space Physics) 114, A05204.

Turunen, E., Verronen, P.T., Seppälä, A., Rodger, C.J., Clilverd, M.A., Tamminen, J., Enell, C.F., Ulich, T., 2009. Impact of different energies of precipitating particles on NO_x generation in the middle and upper atmosphere during geomagnetic storms. Journal of Atmospheric and Solar-Terrestrial Physics 71, 1176–1189.

Calculation of the magnetospheric structure during substorm growth phase using satellite observed pressure: Initial results

Liheng Zheng

Department of Physics and Astronomy, Rice University, Houston, TX

Sorin Zaharia

Space Science and Applications, Los Alamos National Laboratory, Los Alamos, NM

Frank Toffoletto

Department of Physics and Astronomy, Rice University, Houston, TX

Chih-Ping Wang

Department of Atmospheric and Oceanic Sciences, University of California, Los Angeles, CA

Abstract

To understand the onset mechanism of magnetospheric substorms one needs the ability to link disparate magnetospheric and ionospheric observations during the substorm growth phase. This connection is through mapping along magnetic field lines, however current models [either empirical or magnetohydrodynamic (MHD)] are unable to accurately describe the magnetic field during the growth phase. To solve this problem, a first principle calculation of magnetospheric equilibrium with prescribed initial and boundary conditions is utilized to study the specific magnetic field configurations during the growth phase. In this report, we describe the initial results obtained from the magneto-friction equilibrium code with the pressure obtained from observations made by the Time History of Events and Macroscale Interaction during Substorms (THEMIS) and Geotail probes. These results are also compared with those of the LANL 3D Euler potential equilibrium code, to evaluate the relative strengths and weaknesses of the 2 equilibrium approaches. The global magnetospheric equilibrium calculated by the magneto-friction code may be used to provide more realistic initial and boundary conditions for the LANL 3D code in the future, thus to produce better than ever magnetosphere equilibria.

Citation: Zheng, L., S. Zaharia, F. Toffoletto and C.-P. Wang (2011), Calculation of the magnetospheric structure during substorm growth phase using satellite observed pressure: Initial results, Los Alamos Space Weather Summer School Reports 2011, pp. 34–43, LA-UR 12-00074, ISBN 978-0-9850208-1-1

Keywords: magnetospheric equilibrium, substorm growth phase, magneto-friction code, LANL 3D code

1. Introduction

In the study of the onset mechanism of magnetospheric substorms, it is often desired to have knowledge of the magnetic field to map along field lines from the ionosphere through the plasma sheet, in order to link the disparate observations made by ground-based observatories and spacecraft, and to determine their relative positions. During the substorm growth phase, the cross-tail current sheet is greatly thinned and intensified compared to quiet times [e.g., Sergeev et al., 1990; Sanny et al., 1994], and magnetotail field lines are stretched as a result. On the other hand, quasi-static equilibrium still holds during the growth phase [Voigt and Wolf, 1988], therefore, the magnetic field must also satisfy (approximate) force balance with plasma pressure. These two restrictions make it inadequate to map magnetic field lines using nowadays well-established magnetic field models during growth phase, because empirical models,

Email addresses: zhengliheng@rice.edu (Liheng Zheng), szaharia@lanl.gov (Sorin Zaharia), toffo@rice.edu (Frank Toffoletto), cat@atmos.ucla.edu (Chih-Ping Wang)

such as Tsyganenko 96 magnetic field model (T96) [Tsyganenko and Stern, 1996], were obtained from statistical averages that might not comprise many (relative to the total number) growth phase data points, while global MHD models, such as the Block Adaptive Tree Solar Wind Roe Upwind Scheme (BATS-R-US) [Powell et al., 1999], have difficulty reproducing realistic magnetospheric configurations during specific events.

Efforts have been made to overcome this inadequacy. Kubyshkina et al. [2009] and Kubyshkina et al. [2011] proposed an adapted time-dependent magnetospheric model. In their model, they adapted the empirical model (T96) to spacecraft observations by varying its input parameters to find the best fit to the observed field. Using this method, Sergeev et al. [2011] was able to analyze an isolated substorm growth and expansion on 29 March 2009 by conjugating THEMIS spacecraft observations with simultaneous ground-based measurements. However, this model heavily depends on spacecraft observations during specific events (which might be very few/not available), thus is not quite suitable for the study of substorm growth phase in general. Additionally, it contains no information on the plasma.

In another approach, first principle calculations of magnetospheric equilibria have also been developed. Cheng [1995], Zaharia et al. [2004] and Zaharia [2008] solved the 3 dimensional (3D) plasma equilibrium problem by solving the single-fluid force balance equation $\boldsymbol{J} \times \boldsymbol{B} = \nabla P$ in terms of Euler potentials. Their method (henceforth named the LANL 3D code) is capable of dealing with plasma pressure anisotropy [Zaharia et al., 2006], thus is especially suitable for calculations in the near-Earth magnetosphere. Hesse and Birn [1993], Toffoletto et al. [2001] and Lemon et al. [2003] have successively developed a magneto-friction approach, which relaxes the magnetosphere by artificially introducing friction and viscosity into the ideal MHD equations in order to dissipate energy. In this report, we will present initial results for the growth phase magnetospheric structure simulated by both the magneto-friction method and the LANL 3D code, with the aid of particle data from THEMIS and Geotail spacecraft observations.

2. Magnetospheric equilibrium solver: the magneto-friction code

2.1. Theoretical background

Except for highly dynamic times such as substorm expansion phase, plasma convection speeds in the magnetosphere are very small compared to the MHD wave speeds, and the characteristic flow times are thus very long compared to the travel time of signals between ionosphere and the plasma sheet. This requires, in the MHD equations, the flow speed $\boldsymbol{v}$ and quantities generated by $\partial/\partial t$ to be first order quantities compared to the zeroth order pressure, density, current and magnetic field. Consequently, the inertial term (left-hand side) in the single-fluid plasma momentum equation

$$\rho\left[\frac{\partial \boldsymbol{v}}{\partial t} + (\boldsymbol{v} \cdot \nabla)\boldsymbol{v}\right] = \boldsymbol{J} \times \boldsymbol{B} - \nabla P \tag{1}$$

becomes a second order quantity and is negligible. The remaining zeroth order MHD equations describe a quasi-static equilibrium in our system, specifically,

$$\boldsymbol{J} \times \boldsymbol{B} = \nabla P \tag{2}$$

$$\nabla \times \boldsymbol{B} = \mu_0 \boldsymbol{J} \tag{3}$$

$$\nabla \cdot \boldsymbol{B} = 0 \tag{4}$$

Chodura and Schlüter [1981] demonstrated that, in an MHD system, a minimum of the system's potential energy implies the MHD force density $\boldsymbol{J} \times \boldsymbol{B} - \nabla P$ vanishing everywhere. Therefore, a minimal potential state is also an equilibrium state. To dissipate energy, Hesse and Birn [1993] added a viscous term and a frictional term into the MHD momentum equation (1), namely,

$$\rho\frac{d\boldsymbol{v}}{dt} = \boldsymbol{J} \times \boldsymbol{B} - \nabla P + \nu\nabla^2\boldsymbol{v} - \alpha\rho\boldsymbol{v} \tag{5}$$

where ν is the viscosity coefficient and α the friction coefficient. The minimal potential energy state is approached as the system evolves in this modified MHD manner, and the rate of total energy change is given by,

$$\frac{d}{dt}\int_V dV\left(\frac{B^2}{2\mu_0} + \frac{1}{2}\rho v^2 + \frac{P}{\gamma - 1}\right) = \int_V dV\left(-\alpha\rho v^2 + \nu\boldsymbol{v} \cdot \nabla^2\boldsymbol{v}\right) \tag{6}$$

As long as the right-hand side of equation (6) is negative, energy is continuously dissipated from the system. And finally, as the flow velocity approaches zero, the dissipation also vanishes. It should be mentioned that, although such

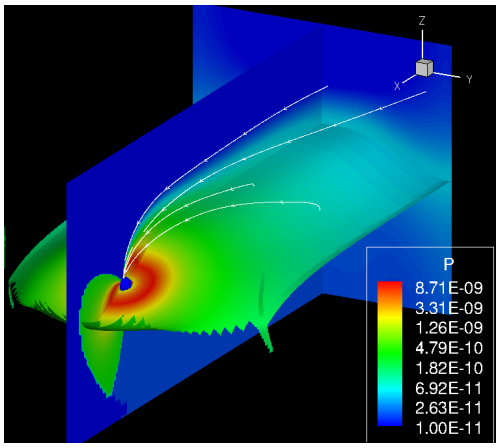

Figure 1: Slice view of the friction code computational domain. Shown in this figure are the pressure distributions in the noon-midnight meridian plane, the neutral sheet, and the tailward boundary, as populated by Tsyganenko Mukai 2003 model (TM03) [Tsyganenko and Mukai, 2003] with extrapolation near the Earth. Earth is represented by the small blue ball located in the lower left region. Magnetic field is determined by T96 with a 30° dipole tilt, thus making the neutral sheet a curved surface. The neutral sheet is located by the places where the horizontal component of magnetic field reverses in the magnetosphere, and its ragged edge is caused by the encountering with magnetopause. White lines stemming from the Earth illustrate two types of magnetic field line tracings: going across the neutral sheet and ending on the tailward boundary.

an evolution process may never have happened in nature, the final lowest potential state does not depend on the actual evolutional path the system takes, except for the different choices of γ value [Hesse and Birn, 1993]. For various γ values, the equilibrium solution is however not unique. The higher value γ takes, the less compressible the fluid would be [Wolf et al., 2006].

2.2. The magneto-friction code

Using the mechanism described in subsection 2.1, the magneto-friction code (hence abbreviated the friction code) seeks the magnetospheric equilibrium by evolving the suite of MHD equations modified with artificial friction and viscosity in "time" in a 3D variable density Cartesian grid space [Lemon et al., 2003]. Note that, "time" in the friction code is not physical, but rather a name of the iterative steps. The computational domain, as shown in Figure 1, encloses the magnetopause on the dayside, extends to as far as $-50\ R_E$ in the magnetotail, and expands to $\sim \pm 15 R_E$ in geocentric solar magnetic (GSM) Y and Z direction. The friction code is able to treat arbitrary dipole tilts and interplanetary magnetic field (IMF) polarities.

The initial setup of the code depends on externally provided 3D magnetic field profiles and neutral sheet pressure distribution, either empirical or results from other sources. To initialize pressure at every grid node, the friction code traces the magnetic field line threading the grid node to the neutral sheet (see Figure 1), and sets the initial pressure at the node the same as that at the field line's neutral sheet crossing position, since from equation (2) the pressure is constant along a field line when a force balance is presumed. For tail lobe field lines, which do not cross the neutral sheet, the friction code first calculates an initial pressure distribution on the tailward boundary of the domain by integration of the force balance equation (2) along Z direction from the neutral sheet, with $\boldsymbol{J}$ expressed by the magnetic field according to Ampère's law (3), that is, it solves for $P(x_0, y_0, z)$ by

$$\left(P + \frac{1}{2\mu_0}B^2\right)\Big|_{(x_0,y_0,z)} = \frac{1}{\mu_0}\int_{z_0}^{z} \left[\boldsymbol{B}\left(x_0, y_0, \zeta\right)\cdot\nabla\right] B_z(x_0, y_0, \zeta)\, d\zeta + \left(P + \frac{1}{2\mu_0}B^2\right)\Big|_{(x_0,y_0,z_0)} \tag{7}$$

where x_0, y_0 and z_0 are coordinates of positions in the neutral sheet, and $\boldsymbol{B}(x, y, z)$ is a known function provided by the initial magnetic field. Then, the pressure on the field line is set as $P(x_0, y_0, z)$.

Figure 2 shows the residual force density $|\boldsymbol{J}\times\boldsymbol{B} - \nabla P|$ distributions in the initial setup and the final relaxed state after 2000 iterations, with $\gamma = 5/3$ for the relaxation procedure. Initially, the imbalanced force density is relatively larger in the inner magnetosphere and the plasma sheet. In the final state, the tail lobes are nearly force free, and force

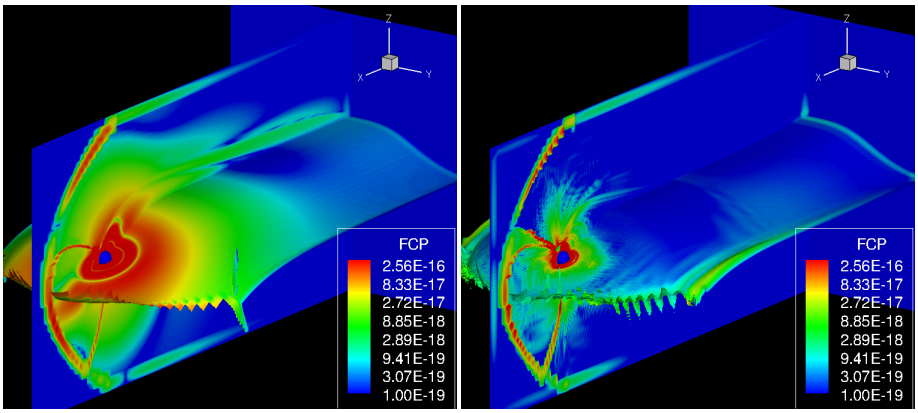

(a) Initial residual force density (b) Residual force density after 2000 iterations

Figure 2: Comparison of residual force densities between the initial state and the final state (relaxed with $\gamma = 5/3$) computed by the friction code. Color maps show the logarithmic scale of the absolute values of force density, in unit of N/m^3, in the noon-midnight meridian plane, the tailward boundary and the neutral sheet. Across the magnetopause and the polar cusps, MHD force balance does not exist. Therefore, the positions of magnetopause and polar cusps are clearly seen as red curves in the left region of each panel.

density in the plasma sheet has been reduced by about two orders of magnitude, and that in the inner magnetosphere by about one order of magnitude. Near the boundaries, force imbalance has not changed much – this is the boundary effect of the friction code. Noticeably, the shape of the curved neutral sheet changes too as a result of relaxed magnetic field, despite that its intersections with computational domain boundaries are fixed.

Figure 3 plots the temporal variations of volume integrated residual force density, kinetic energy and total potential energy during a typical relaxation procedure. In Figure 3(a), residual force drops by more than one order of magnitude compared to its initial level. It decays quickly in the first a few hundred iterations, and after that slowly approaches a final level. In Figure 3(b), kinetic energy increases immediately when the system is allowed to relax from its initial state, and is then sharply cut to zero because the code detects a peak of it, which corresponds to a local minimum of potential along the evolutional path, and halts the entire system at this moment by setting all velocities to zero. Afterwards, the relaxation is restarted from this metastable state. This is the so called "ballistic method" [Hesse and Birn, 1993], which is designed to prevent the calculation from being wasted on oscillations around metastable states. Figure 3(c) shows that the total potential energy indeed decreases as designed. Fluctuations within the first few hundred iterations might be an effect of the grid scale noise in the calculation.

3. Substorm growth phase magnetospheric structure

In this study, we reconstruct the substorm growth phase magnetosphere by calculating magnetospheric equilibrium from substorm growth phase pressure observed by THEMIS and Geotail spacecraft. Data were selected from time periods with $AE < 200\ nT$ within 30 minutes prior to substorm onsets. Figure 4 illustrates the selection criterion and plots respectively the number of data points, neutral sheet pressure and magnetic field Z component in GSM equatorial plane on a mesh with grid scale 1 R_E. As expected for substorm growth phase, B_z exhibits a minimum around $-20\ R_E$ in the tail, with magnitude as small as 1 nT.

We initialize the friction code using the observed equatorial pressure profile, with blank spots extrapolated according to the Spence-Kivelson pressure model [Spence et al., 1989], and magnetic field using Tsyganenko 89 model (T89) [Tsyganenko, 1989] with $K_p = 3$, which was determined by the averaged K_p values from the observations. We choose $\gamma = 1$ rather than a larger value for the relaxation, which corresponds to an isobaric procedure, because we have more confidence in the observed pressure and want the magnetic field to adjust more. Figure 5 shows the initial and final states (after 1500 iterations) of the equilibrium calculation, and the field line stretching on a geostationary Earth orbit (GEO). Comparing Figure 5(b) with 5(a), the pressure "noise" in the equatorial plane in the initial state is smoothed as a result of the relaxation; tail field lines in the plasma sheet become more stretched. The inner magneto-

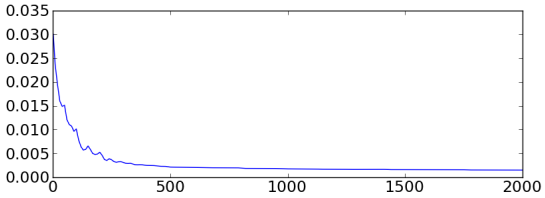

(a) Integrated residual force density

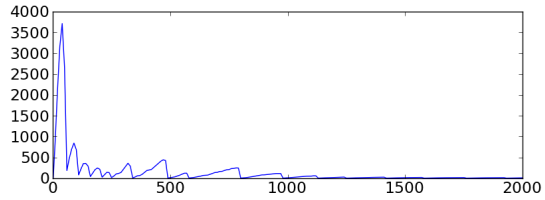

(b) Integrated kinetic energy

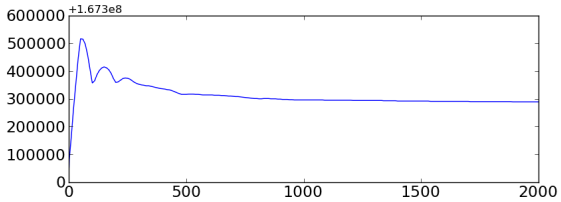

(c) Integrated total potential energy

Figure 3: Temporal variations of integrated force density, kinetic energy and potential energy of a typical friction code relaxation. The horizontal axis of each panel shows the iteration steps. Data in these curves are in code normalized units, thus only their relative values are meaningful. Note in Panel (c), the absolute values on the vertical axis are 1.673×10^8 plus the tick mark values. The change in total potential energy is very small compared to its absolute value.

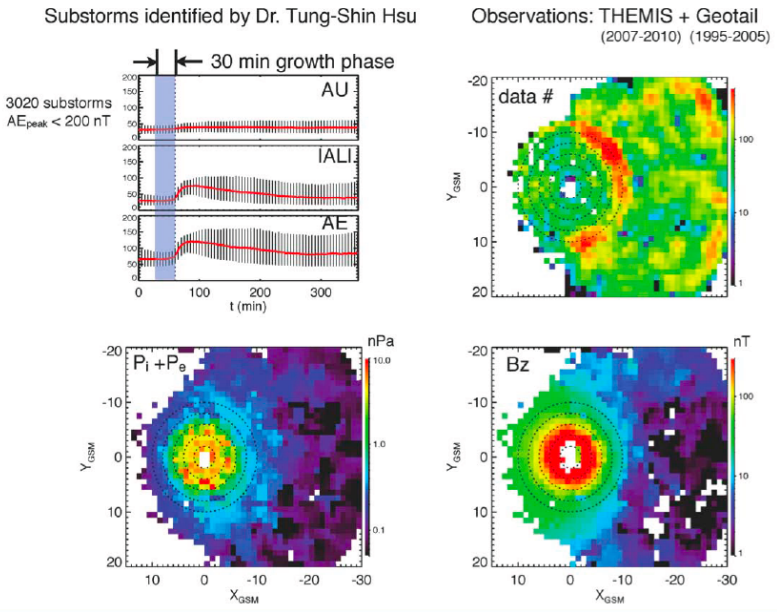

Figure 4: Substorm growth phase observations by THEMIS and Geotail. Upper left panel illustrates our growth phase data selection criterion. Upper right panel shows the number of satellite observations within each grid square. Lower row panels draw the observed neutral sheet thermal pressure and B_z respectively. Blank spots mean no data available.

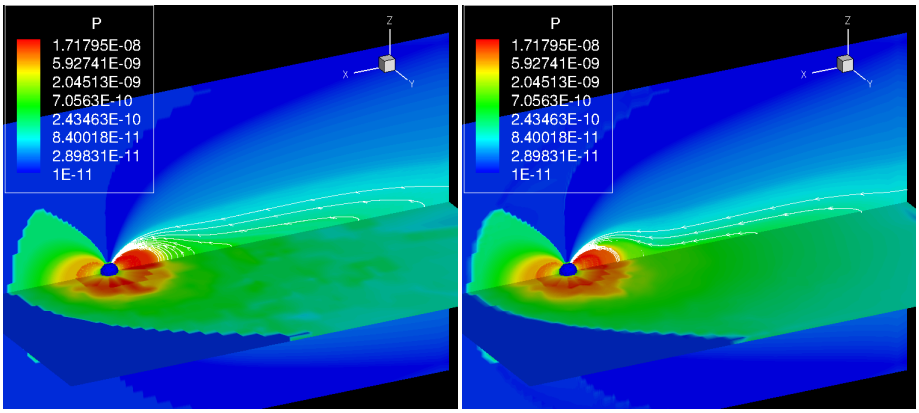

(a) Initial pressure and magnetic field (b) Force balanced pressure and magnetic field

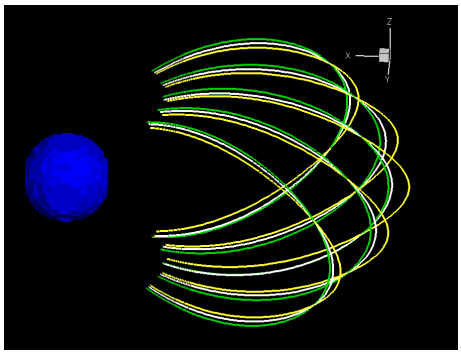

(c) Field line stretching on GEO

Figure 5: Initial and final states of the equilibrium calculation. In panels (a) and (b), pressure is plotted in logarithmic scale with unit *Pa*. Panel (c) shows the comparison of magnetic field lines through the same GEO under different conditions. The geosynchronous orbit plane is tilted 23.5° toward the Sun with respect to magnetic equatorial plane. Green lines are field lines of T89 with $K_p = 0$. They represent the averaged quiet time field line shapes. White lines are field lines of T89 with $K_p = 3$, which are the field lines in our initial setup. The most stretched yellow lines are field lines in the final equilibrated state.

sphere field lines have also been stretched. Compared to the quiet time configuration in T89, the equatorial crossing point of the field line through GEO at midnight extends $\sim 0.5\ R_E$ tailward (Figure 5(c)).

Figure 6 depicts the equilibrium equatorial B_z profile from both the friction code and the LANL 3D code results. The LANL 3D code result was calculated with the same initial magnetic field model, but with smoothed initial pressure by fitting an empirical formula against the observed data, because grid scale noise in data could cause trouble to the code. Comparing with observed B_z in Figure 4, both codes obtain the broad B_z minimum in the tail around midnight, whereas the friction code result even resolves some of the fine structures in the flanks. A comparison of B_z along the $-X$ axis between observation and different models is shown in Figure 7. Tailward of $-15\ R_E$, both the friction code and the LANL 3D code results reveal close resemblance of observation, and are better than empirical models. However, the friction code result deviates from both data and the LANL 3D curve by having a deep minimum of B_z at about $-10\ R_E$. This B_z configuration is more likely to occur in the late growth phase, while our observation time period spans a full 30 minutes before onset. We note that the adiabatic plasma convection theory predicts that a B_z minimum should occur at the edge of the entropy parameter $PV^{5/3}$ plateau due to conservation of entropy along convection paths [Voigt and Wolf, 1988]. Figure 8 plots the equatorial $PV^{5/3}$ distribution from the two methods. In the friction code result [Figure 8(a)], we can see a clear plateau of roughly constant $PV^{5/3}$ (green color) in the mid-tail, whose inner edge at midnight is at about $-10\ R_E$, right at the place the minimum B_z occurs. In the LANL 3D code result [Figure 8(b)], the plateau is not obvious. Further down the tail, $PV^{5/3}$ increases dramatically. The observed non-conservation of $PV^{5/3}$ was named the "entropy crisis" by Wolf et al. [2009], and was explained there by the movement of bubble

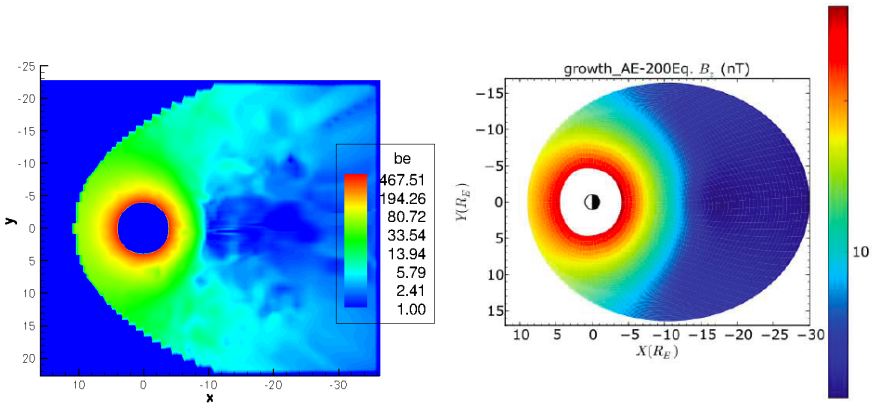

(a) Equatorial B_z (nT) from friction code result (b) Equatorial B_z from LANL 3D code result

Figure 6: Equilibrium equatorial B_z from friction code and the LANL 3D code.

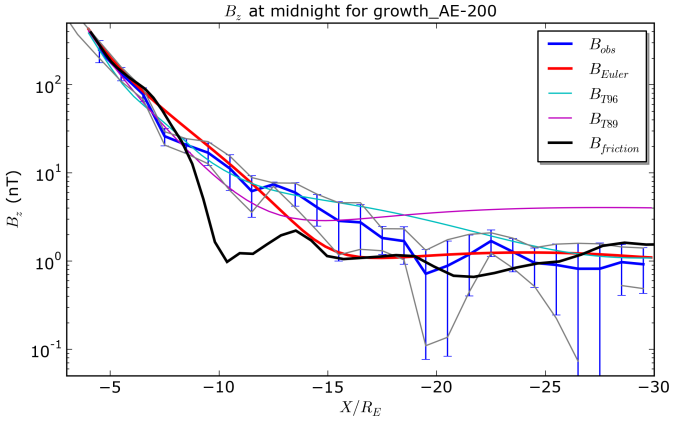

Figure 7: B_z along $-X$ axis for growth phase. The thick blue curve with error bar shows the observed data. The thick black curve is the friction code result. The thick red curve is the LANL 3D code result. For reference, the thin purple curve shows midnight B_z from T89, and the thin cyan curve from T96. Noticeably, the friction code result has a deep minimum at about $-10\ R_E$.

and blobs, as well as the effect of curvature and gradient drifts in the near-Earth magnetosphere.

We have also calculated field-aligned current (FAC) and perpendicular current for the equilibrium states of both methods. In both codes, the FAC is calculated by integrating Vasyliunas equation in differential form,

$$B\frac{\partial}{\partial s}\left(\frac{J_\parallel}{B}\right) = \frac{(\nabla B^2 \times \boldsymbol{B})\cdot\nabla P}{B^4} \tag{8}$$

from neutral sheet to one ionosphere [Vasyliunas, 1984; Cheng, 1995], where s denotes arc length along a field line. The results of FAC are plotted in Figure 9. Both methods have obtained strong Region-2 FAC, whose magnitude on the order of 1 $\mu A/m^2$, which is consistent with Iridium observations [Anderson et al., 2008]. The peak values of FAC are both about 8 $\mu A/m^2$ located in the pre-midnight local time sector. The LANL 3D code current wedge is only slightly southward of the 70° magnetic latitude, whereas the friction code result is 2° $\sim$ 3° more equatorward, indicating that the friction code magnetic field lines are more stretched. The perpendicular current is calculated from

$$\boldsymbol{J}_\perp = \frac{\boldsymbol{B}\times\nabla P}{B^2} \tag{9}$$

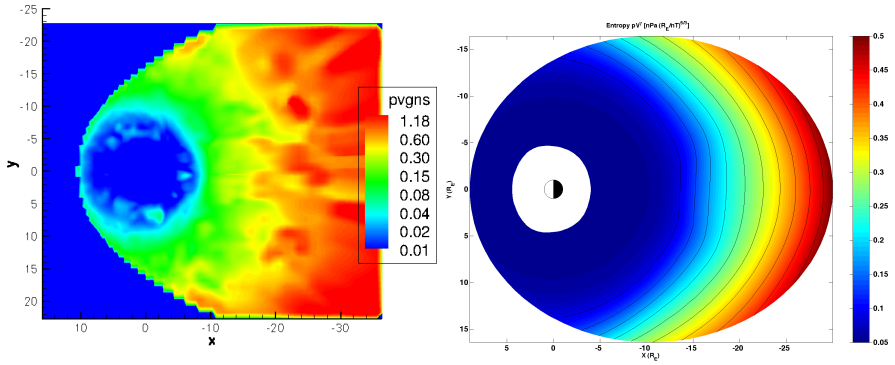

(a) Equatorial $PV^{5/3}$ from friction code result (b) Equatorial $PV^{5/3}$ from LANL 3D code result

Figure 8: Equilibrium equatorial $PV^{5/3}$ from the friction code and the LANL 3D code. The unit of $PV^{5/3}$ is $nPa(R_E/nT)^{5/3}$.

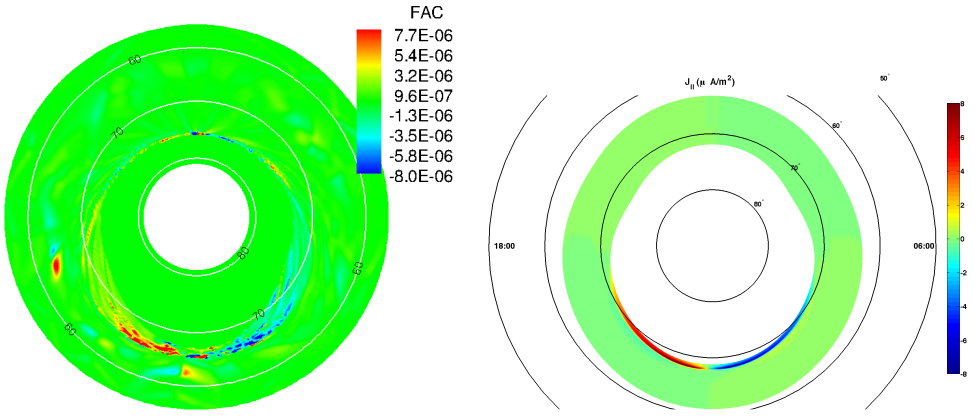

(a) Region 2 FAC calculated by the friction code (b) Region 2 FAC calculated by the LANL 3D code

Figure 9: Field-aligned current calculated by the two methods as plotted in linear scale in the northern ionosphere. Positive values mean the current is flowing into the ionosphere. Local noon is on the top of the circle in each panel. In Panel 9(a), the dayside "current" located on the edge of polar cap results from the last closed field lines in the northern polar cusp. Lower latitude sporadic spots are caused by the noise in pressure data.

and the friction code results are illustrated in Figure 10. A close scrutiny of the ring current in Figures 10(b) and 10(c) reveals a thin eastward ring current inside of the inner magnetosphere pressure peak. In the tail, the current sheet density intensifies by two orders of magnitude and its half thickness thins from more than 1 R_E to about $\sim$ 0.4 R_E at midnight at -15 R_E. In the near tail region, one can also see the phenomenon of current sheet bifurcation toward north and south, as described by Birn et al. [2009].

4. Conclusive remarks

Using THEMIS and Geotail substorm growth phase pressure data, we have successfully calculated with the friction code and the LANL 3D code the force balanced state of the magnetosphere during a typical substorm growth phase. The equilibrated magnetosphere displays the following structures that are characteristic of a substorm growth phase: (1), nightside magnetic field lines are stretched compared to empirical models, both in the tail and near to the Earth; (2), an entropy parameter plateau is observed in the friction code results, and the entropy distribution is consistent with adiabatic convection theory; (3), stronger and more realistic (than portrayed by empirical models) field-aligned current, cross-tail current and ring current are obtained.

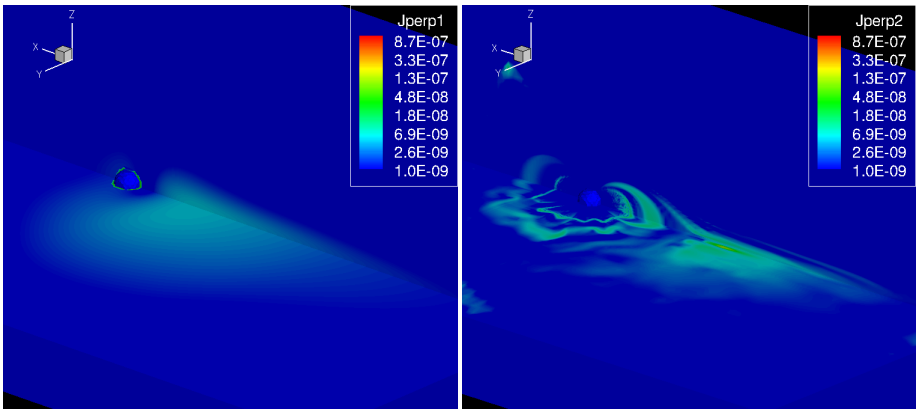

(a) Perpendicular current in T89

(b) Perpendicular current in the equilibrium state

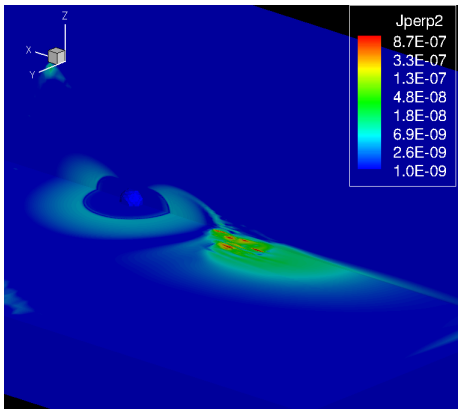

(c) Perpendicular current in the equilibrium state calculated from smoothed pressure

Figure 10: Perpendicular current in the friction code result. As a reference, panel (a) shows the perpendicular current calculated by Ampère's law in the initial T89 magnetic field. The maximal cross-tail current density is about 10^{-3} $\mu A/m^2$. Panel (b) shows the perpendicular current in the friction code equilibrium state. Compared to the initial state, the current sheet half thickness reduces to ~ 0.4 R_E at midnight at -15 R_E, and the peak current density is about 0.1 $\mu A/m^2$. One can also clearly see a ring current in the inner magnetosphere. Panel (c) shows the result of a different friction code run with smoothed initial pressure profile. The current sheet is even thinner and stronger in this result, and the ring current appears smooth and symmetric.

In calculating magnetospheric equilibrium, the friction code and the LANL 3D code have their respective strengths and weaknesses. The friction code method is able to deal with tail lobe field lines, hence is more flexible with computational domain sizes and initial magnetic field conditions. The friction code is more robust with noises in the initial pressure. However, compared to the LANL 3D code result, the friction code resultant magnetotail field lines are more stretched, and perhaps over stretched by having a B_z minimum in the near Earth tail that is absent in both observation and the LANL 3D result. In some cases, the tail field lines could be so stretched that numerical diffusion intrinsic to the friction code's algorithm will violate the "frozen-in flux" condition of ideal MHD and trigger numerical magnetic reconnection in the tail. We have not yet found a means to overcome this problem. However, Birn and Schindler [2002] and Birn et al. [2004] have demonstrated using quasi-static equilibrium theory that, subject to certain supercritical finite boundary deformations, for certain configurations equilibrium solutions may no longer exist in the magnetosphere. This could possibly suggest an explanation to our problem. Finally, as the LANL 3D code is excellent in calculating near-Earth magnetosphere equilibrium, whereas the friction code's strength is in the farther tail, a coupling of the two methods may provide promising results in the future.

References

Anderson, B.J., Korth, H., Waters, C.L., Green, D.L., Stauning, P., 2008. Statistical Birkeland current distributions from magnetic field observations by the Iridium constellation. Annales Geophysicae 26, 671–687.

Birn, J., Dorelli, J.C., Hesse, M., Schindler, K., 2004. Thin current sheets and loss of equilibrium: Three-dimensional theory and simulations. Journal of Geophysical Research (Space Physics) 109, A02215.

Birn, J., Hesse, M., Schindler, K., Zaharia, S., 2009. Role of entropy in magnetotail dynamics. Journal of Geophysical Research 144.

Birn, J., Schindler, K., 2002. Thin current sheets in the magnetotail and the loss of equilibrium. Journal of Geophysical Research (Space Physics) 107, 1117.

Cheng, C.Z., 1995. Three-dimensional magnetospheric equilibrium with isotropic pressure. Geophysical Research Letters 22, 2401–2404.

Chodura, R., Schlüter, A., 1981. A 3D code for MHD equilibrium and stability. Journal of Computational Physics 41, 68–88.

Hesse, M., Birn, J., 1993. Three-dimensional magnetotail equilibria by numerical relaxation techniques. Journal of Geophysical Research 98, 3973–3982.

Kubyshkina, M., Sergeev, V., Tsyganenko, N., Angelopoulos, V., Runov, A., Donovan, E., Singer, H., Auster, U., Baumjohann, W., 2011. Time-dependent magnetospheric configuration and breakup mapping during a substorm. Journal of Geophysical Research 116.

Kubyshkina, M., Sergeev, V., Tsyganenko, N., Angelopoulos, V., Runov, A., Singer, H., Glassmeier, K.H., Auster, H.U., Baumjohann, W., 2009. Toward adapted time-dependent magnetospheric models: A simple approach based on tuning the standard model. Journal of Geophysical Research 114.

Lemon, C., Toffoletto, F., Hesse, M., Birn, J., 2003. Computing magnetospheric force equilibria. Journal of Geophysical Research 108.

Powell, K.G., Roe, P.L., Linde, T.J., Gombosi, T.I., Zeeuw, D.L.D., 1999. A solution-adaptive upwind scheme for ideal magnetohydrodynamics. Journal of Computational Physics 154, 284–309.

Sanny, J., McPherron, R.L., Russell, C.T., Baker, D.N., Pulkkinen, T.I., Nishida, A., 1994. Growth-phase thinning of the near-Earth current sheet during the CDAW 6 substorm. Journal of Geophysical Research 99, 5805–5816.

Sergeev, V., Angelopoulos, V., Kubyshkina, M., Donovan, E., Zhou, X.Z., Runov, A., Singer, H., McFadden, J., Nakamura, R., 2011. Substorm growth and expansion onset as observed with ideal ground-spacecraft THEMIS coverage. Journal of Geophysical Research 116.

Sergeev, V.A., Tanskanen, P., Mursula, K., Korth, A., Elphic, R.C., 1990. Current sheet thickness in the near-Earth plasma sheet during substorm growth phase. Journal of Geophysical Research 95, 3819–3828.

Spence, H.E., Kivelson, M.G., Walker, R.J., 1989. Magnetospheric plasma pressures in the midnight meridian: Observations from 2.5 to 35 R_E. Journal of Geophysical Research 94, 5264–5272.

Toffoletto, F.R., Spiro, R.W., Wolf, R.A., Birn, J., Hesse, M., 2001. Modeling inner magnetospheric electrodynamics. Geophysical monograph 125, 265–272. Eng.

Tsyganenko, N.A., 1989. A magnetospheric magnetic field model with a warped tail current sheet. Planet. Space Sci. 37, 5–20.

Tsyganenko, N.A., Mukai, T., 2003. Tail plasma sheet models derived from Geotail particle data. Journal of Geophysical Research 108.

Tsyganenko, N.A., Stern, D.P., 1996. Modeling the global magnetic field of the large-scale birkeland current systems. Journal of Geophysical Research 101, 27,187–27,198.

Vasyliunas, V.M., 1984. Fundamentals of current description, in: Potemra, T. A. (Ed.), Magnetospheric Currents, pp. 63–66.

Voigt, G.H., Wolf, R.A., 1988. Quasi-static magnetospheric MHD processes and the "ground state" of the magnetosphere. Reviews of Geophysics 26, 823–843.

Wolf, R.A., Kumar, V., Toffoletto, F.R., Erickson, G.M., Savoie, A.M., Chen, C.X., Lemon, C.L., 2006. Estimating local plasma sheet $PV^{5/3}$ from single-spacecraft measurements. Journal of Geophysical Research 111.

Wolf, R.A., Wan, Y., Xing, X., Zhang, J.C., Sazykin, S., 2009. Entropy and plasma sheet transport. Journal of Geophysical Research 114.

Zaharia, S., 2008. Improved Euler potential method for three-dimensional magnetospheric equilibrium. Journal of Geophysical Research (Space Physics) 113, A08221.

Zaharia, S., Cheng, C.Z., Maezawa, K., 2004. 3-D force-balanced magnetospheric configurations. Annales Geophysicae 22, 251–265.

Zaharia, S., Jordanova, V.K., Thomsen, M.F., Reeves, G.D., 2006. Self-consistent modeling of magnetic fields and plasmas in the inner magnetosphere: Application to a geomagnetic storm. Journal of Geophysical Research (Space Physics) 111, A11S14.

Los Alamos Space Weather Summer School
30 Bikini Atoll Rd, ISR-1, MS D466
Los Alamos, NM 87545

http://SpaceWeatherSchool.org

ISBN 978-0-9850208-1-1